Temperature and genetic background drive mobilization of diverse transposable elements in a critical human fungal pathogen

Anna I. Mackey[a], Vesper Fraunfelter[a], Samantha Shaltz[a], John McCormick[b], Callan Schroeder[a], John R. Perfect[c], Cedric Feschotte[b], Paul M. Magwene[d], Asiya Gusa[a]

[a]Department of Molecular Genetics and Microbiology, Duke University, Durham, NC, 27701, USA.

[b]Department of Molecular Biology and Genetics, Cornell University, Ithaca, NY, 14850.

[c]Department of Medicine, Duke University, Durham, NC, 27710, USA.

[d]Department of Biology, Duke University, Durham, NC, 27710, USA.

***correspondence**: asiya.gusa@duke.edu

ABSTRACT

Transposable elements (TEs) are key agents of genome evolution across all domains of life. These mobile genetic elements can cause mutations through transposition or by promoting structural rearrangements. Stress conditions can amplify TE activity, either by impairing TE suppression mechanisms or through stress-induced interactions between transcription factors and TE sequences, offering a route for rapid genetic change. As such, TEs represent an important source of adaptability within populations. To investigate the interplay between environmental stress and eukaryotic TE dynamics relevant to infectious disease, we examined how heat stress and nutrient limitation affect TE mobility in the human fungal pathogen *Cryptococcus neoformans*, using a collection of clinical and environmental isolates. Seven distinct mobile element families, encompassing diverse retrotransposons and DNA transposons, were captured mobilizing to confer antifungal resistance, including a novel element, CNEST, which belongs to the CACTA, Mirage, Chapaev (CMC) supergroup. Heat stress at human body temperature (37°C) significantly increased the mobilization of a subset of these TEs, leading to higher rates of acquired antifungal resistance. Whole-genome assemblies revealed that,

compared to retrotransposons, DNA transposons were hypomethylated and approximately uniformly distributed throughout the genome, features that may contribute to their frequent mobilization. We further assessed TE-driven genomic changes within hosts using serial isolates from patients with recurrent cryptococcal infections and from isolates passaged through mice. While we observed evidence of TE copy number changes near chromosome ends, we found no indication of TE-mediated alterations near gene-coding regions across any of the serial isolates. Finally, TE mobility was isolate- and strain-dependent, with significant variation even among clonally related isolates collected from the same patient, emphasizing the role of genetic background in shaping TE activity. Together, these findings reveal a complex, dynamic relationship between environmental stress, genetic background, and TE mobility, with important implications for adaptation and acquired antifungal resistance in *C. neoformans*.

INTRODUCTION

Transposable elements (TEs) are powerful drivers of genomic change and provide a mechanism for adaptive evolution in fungal pathogens (1–8). TEs are mobile genetic elements that fall into two broad categories: class I retrotransposons, which mobilize via an RNA intermediate through a “copy-and-paste” mechanism, and class II DNA transposons, which mobilize via a DNA intermediate, typically through a “cut-and-paste” mechanism (9). TE activity can lead to genomic instability through unchecked transposition or by providing homologous sequences throughout the genome that promote rearrangements (10). However, TEs can also promote beneficial genetic changes, especially under changing or stressful environmental conditions, by modulating the expression of nearby genes, disrupting endogenous gene functions, or providing beneficial cargo (10–14). TE-mediated genetic changes in fungi have been linked to various adaptive phenotypes, including increased fitness under heavy metal stress in *Schizosaccharomyces pombe* and nitrogen-limited conditions in *Saccharomyces cerevisiae* (1–5). Additionally, various stressors can increase TE expression and mobilization rates (14–17).

Diverse TEs are present in *Cryptococcus neoformans*, a human fungal pathogen which primarily causes disease in immunocompromised individuals such as cancer patients, organ transplant recipients, and people living with HIV/AIDS (18–20). *C. neoformans* is responsible for approximately 147,000 deaths annually and accounts for up to 20% of AIDS-related mortality (21,22). It is a ubiquitous environmental yeast, and inhalation of spores or desiccated yeast cells

62 can lead to pulmonary infection that may disseminate across the blood-brain barrier, causing
63 cryptococcal meningitis (18). Approximately 10 – 20% of patients diagnosed with cryptococcal
64 meningitis experience recurrent disease, which can persist for years despite antifungal
65 treatment (23). In-host microevolution can result in adaptive genetic changes that enhance
66 antifungal resistance, alter virulence traits, or increase overall pathogenicity, contributing to
67 persistent infections and treatment failure (24–27). Although in-host microevolution influences
68 disease outcomes, the genetic basis of altered virulence traits and antifungal resistance often
69 remains unknown, potentially because short-read sequencing and variant calling, the primary
70 detection methods, are less suited for identifying structural rearrangements and TE
71 polymorphisms (28).

72 During infection, *C. neoformans* encounters a variety of stressors during the
73 environment-to-host transition. These include shifts in nutrient availability, pH, exposure to
74 reactive oxygen species (ROS), and elevated temperature (37°C) (29). Previous studies in the
75 less pathogenic sister species *Cryptococcus deneoformans* have shown that heat stress
76 significantly increases TE mobilization rates, exceeding those of single nucleotide
77 polymorphisms (SNPs) and insertions/deletions (indels) by more than threefold per generation
78 during in vitro passaging at 37°C (30,31). These findings suggest that in stressful environments,
79 TEs can be the primary drivers of genomic change. Indeed, TE mobilization in *C. deneoformans*
80 has been observed during murine host infection and, in both *C. neoformans* and *C.*
81 *deneoformans*, has been linked to the development of resistance to 5-fluorocytosine (5-FC), a
82 first-line antifungal treatment (30–32). However, it is not known whether heat stress increases
83 TE mobilization rates in *C. neoformans*, which is responsible for approximately 95% of
84 cryptococcal infections (33), and whether TEs contribute to genetic changes accumulated
85 during persistent human infection.

86 *C. neoformans* is known to harbor a variety of TEs, including DNA transposons as well
87 as long terminal repeat (LTR) and non-LTR retrotransposons (19,20). The best-characterized TE
88 suppression mechanism in *C. neoformans* is RNA interference (RNAi). Through this pathway,
89 transcripts targeted for silencing are processed into small interfering RNAs (siRNAs), which are
90 loaded into the RNA-induced silencing complex (RISC) to target homologous transcripts for
91 degradation (34–37). RNAi has been shown to silence double-stranded RNAs, transcripts with
92 sub-optimal splicing signals, repetitive transgenes, and TEs in *C. neoformans* (34,35,37,38).
93 Unlike in the yeast *S. pombe*, RNAi is strictly involved in post-transcriptional silencing in *C.*
94 *neoformans* and does not lead to transcriptional silencing by facilitating the assembly or

maintenance of heterochromatin (34). Prior studies have shown that loss-of-function mutations in key RNAi genes can lead to a hypermutator phenotype, driven by rampant TE mobilization, but only in strains with high TE burden (32,38). TE mobilization may also be shaped by epigenetic context. LTR and non-LTR elements are enriched in centromeric and subtelomeric regions (38,39), where they co-localize with epigenetic features of silent chromatin, such as 5-methylcytosine DNA methylation and repressive histone modifications, including H3K27me3 and H3K9me2 (38–42). These marks are also enriched in centromeric and subtelomeric regions, and are rarely detected in gene-rich chromosomes arms (38–42). Despite this association, the regulatory effects of DNA methylation and heterochromatin on TEs in *C. neoformans* remain poorly understood, particularly regarding their influence on the mobilization of active TE families.

In this study, we investigated how stressors encountered during human infection, including elevated temperature and limited nutrient availability, influence TE mobilization in *C. neoformans*. Using a reporter gene-based approach, we examined TE mobility in genetically diverse clinical and environmental isolates, including representatives from three of the four major lineages (VNI, VNII, and VNBII) (43). We found diverse, active TEs in *C. neoformans*, including several whose identity or mobility were previously unknown. TE mobility was temperature-dependent for all elements assessed, with heat stress significantly increasing transposition rates for a subset of elements. De novo telomere-to-telomere genome assemblies were used to examine TE-driven genetic changes in serially collected isolates from patients with recurrent cryptococcal meningitis. Using these assemblies, we annotated TEs to assess the genomic distribution and DNA methylation status of various transposable element types. DNA transposons were approximately uniformly distributed throughout the genome and had significantly reduced levels of DNA methylation compared to retrotransposons. Lastly, we found that TE copy number and mobility were highly isolate- and strain-dependent, suggesting that genetic background is a major determinant of TE-mediated genomic impacts. Together, these results highlight the critical roles of environmental factors, particularly temperature, in driving stress-induced genomic changes and adaptive evolution via transposition in the human fungal pathogen *C. neoformans*.

RESULTS

Diverse transposable elements mobilize in a subset of *C. neoformans* clinical isolates

126 To investigate transposable element (TE) mobilization dynamics in *Cryptococcus*, we
127 obtained a set of 33 clinical isolates from 18 South African patients with recurrent cryptococcal
128 meningitis, collected as part of the GERMS-SA surveillance study (Table S1) (44). Isolates were
129 collected by plating cerebrospinal fluid and selecting a single colony at the time of diagnosis
130 (incident) and after subsequent disease relapse(s), which occurred 57 to 238 days later (Fig 1A,
131 Table S1). Using short read sequencing, a prior study found that isolates collected from the
132 same patient differed by few single nucleotide polymorphisms (SNPs) and insertions/deletions
133 (indels), and that these isolates formed monophyletic clades in phylogenetic analyses,
134 suggesting that disease relapses were clonal and not due to reinfection (24). Isolates are
135 genetically diverse, including *Cryptococcus neoformans* isolates belonging to three of the four
136 major clades, VNI, VNII, and VNBII, and *Cryptococcus gattii* isolates belonging to clades VGI
137 and VGIV (Table S1) (43,45).

138 Prior work from our group showed that growth at 37°C increased TE mobilization rates in the
139 less pathogenic species *Cryptococcus deneoformans* (30,31). To investigate TE activity under
140 heat stress in *C. neoformans* and *C. gattii*, both recognized as priority fungal pathogens by the
141 World Health Organization (46), we conducted a preliminary screen using a “transposon trap”
142 assay that detects mutations in the *FRR1* reporter gene, a system previously used by our group
143 and others (30,32,38). Incident and relapse isolates from the 18 South African cases were
144 cultured in non-selective nutrient-rich YPAD medium at 37°C and plated to medium containing
145 the antifungal drugs rapamycin and FK506 (rap+FK506). Only mutations in *FRR1*, which
146 encodes the shared drug target, can confer resistance to both antifungals (Fig 1B) (47). Ten
147 independent rap+FK506 resistant mutants were collected from each isolate and analyzed by
148 PCR and sequencing to determine the causative mutation of drug resistance. Large DNA
149 insertions, approximately 150 bp – 11 kb, detected by PCR amplification and indicative of TE
150 insertions were confirmed by Sanger sequencing. Isolates from three cases contained TE
151 insertions disrupting the *FRR1* locus at 37°C: cases 7, 15, and 77, which belong to the VNBII,
152 VNI, and VNII clades, respectively (Table 1). TE mobilization was detected exclusively in *C.*
153 *neoformans*; of the three *C. gattii* cases screened, only point mutations were identified in *FRR1*.
154 Subsequent screening of case 7 and 77 isolates at 30°C (see below) detected additional mobile
155 element families.

156 In total, we screened over 1,000 independent rap+FK506-resistant mutants and identified
157 more than 350 independent TE insertion events in *FRR1*. Elements were assigned to known
158 families based on sequence similarity, using Sanger or linear amplicon sequences compared to

159 *C. neoformans* TE family consensus sequences in Repbase, or to GenBank submissions when
160 family-level consensus sequences were unavailable. Family membership was assigned based
161 on the 80-80-80 rule: nucleotide similarity had to exceed 80% over at least 80 base pairs and
162 cover at least 80% of the recovered sequence length (48). An exception to this was the non-LTR
163 retrotransposon CNL1, which shares only ~60% nucleotide similarity with the CNL1 consensus
164 sequence in Repbase. However, it exhibits high (> 99%) nucleotide similarity to an active mobile
165 element previously classified as CNL1 in *C. neoformans* by Priest et al. (2022), so we have
166 retained this name. Additionally, junction PCR was used to identify TE families for a subset of
167 insertion events, employing primers designed to match the internal region of elements
168 previously identified as inserting into *FRR1* in the same isolate. In total, we identified seven
169 diverse TE families mobilizing in *C. neoformans* clinical isolates (Fig 1C). This includes an
170 element belonging to a family that, to our knowledge, has not been identified in previous studies
171 (CNEST), as well as elements not previously reported to be mobile (CNIRT6, TCN3, KDZ3) (Fig
172 1C, Table S2). These elements included DNA transposons (class II), as well as long terminal
173 repeat (LTR) and non-LTR retrotransposons (class I).

174 **CNIRT6 transposition drives increased drug resistance rates at 37°C in case 15**

175 To assess how heat stress impacts rap+FK506 drug resistance rates, fluctuation assays
176 were performed on case 15 incident, relapse, and relapse 2 isolates. All displayed significant
177 increases in rap+FK506 resistance rates during growth at 37°C compared to 30°C in YPAD
178 medium (21-, 12-, and 4-fold, respectively) (Fig 2A). The spectrum of mutations in *FRR1* was
179 obtained by PCR and Sanger or linear amplicon sequencing of independent mutants, followed
180 by mapping to the wild-type *FRR1* sequence for each isolate (Fig S1A). For a subset of
181 insertions, junction PCR was also used. Strikingly, many of the mutations in *FRR1*, up to 91% in
182 the incident isolate at 37°C, were caused by insertions of a large DNA transposon with 99.7%
183 nucleotide similarity to a putative element named CNIRT6 (GenBank: JQ277267.1) (Fig 2B).
184 CNIRT6 was originally identified in *C. neoformans* strain JF289 through sequence analysis,
185 however, this transposon has not been described in the literature and is absent from Repbase.
186 Mapping of a subset of these insertions revealed CNIRT6 transposition into *FRR1* introns and
187 exons, resulting in 3 bp terminal site duplications (TSDs) with variable sequences (Fig S2A, B).
188 CNIRT6 insertion rates were significantly higher at 37°C compared to 30°C, increasing by 28-,
189 20-, and 16-fold in the incident, relapse, and relapse 2 isolates, respectively (Fig 2C). Notably,
190 drug-resistance rates at 37°C and CNIRT6 mobility at both temperatures decreased
191 progressively in relapse isolates collected 166 and 223 days after the incident isolate.

192 Given the significant differences in CNIRT6 mobilization rates among case 15 isolates, we
193 hypothesized that inter-isolate variability may be driven by differences in copy number, genomic
194 position, or epigenetic regulation. To investigate these factors, and to assess all inter-isolate
195 polymorphisms caused by mobile elements, we performed long-read sequencing to generate
196 contiguous, telomere-to-telomere genome assemblies, which were polished with Illumina reads
197 (Table S3). 5-methylcytosine (5mC) DNA methylation was identified using Nanopore signal data.
198 Given that all CNIRT6 insertions into *FRR1* appeared to be the same length by gel
199 electrophoresis and shared high nucleotide similarity to one another (> 99%), the full-length
200 CNIRT6 sequence, obtained by linear amplicon sequencing from an insertion into *FRR1*, was
201 used as the query in BLAST-like alignment tool (BLAT) (49) searches against case 15 genome
202 assemblies to identify full-length copies (Fig S1A). For all BLAT searches predetermined cutoffs
203 of nucleotide identity ≥ 90% and coverage ≥ 95% were used to call full-length copies. This
204 analysis revealed two full-length CNIRT6 copies that are positionally conserved between
205 incident and relapse isolates: one is an exact match to the CNIRT6 sequence identified inserting
206 into *FRR1*, and the second differs by a single nucleotide substitution (Fig 2D). The nucleotide
207 sequences of both CNIRT6 copies are identical between the serial isolates. No DNA methylation
208 was detected in any full-length CNIRT6 copies across all case 15 isolates, as indicated by
209 methylation frequencies < 0.75 at each CpG site, meaning fewer than 75% of long-read signal
210 data supported a methylated call (Table S4). Therefore, differences in genomic copy number,
211 chromosomal location, or DNA methylation do not appear to underlie differences in CNIRT6
212 mobilization rates between serial isolates.

213 To comprehensively assess all genomic changes between case 15 isolates that may have
214 been mediated by TEs other than CNIRT6, we performed synteny and read depth analyses, and
215 used Synteny and Rearrangement Identifier (SyRI) (50), to define structural rearrangements
216 and identify insertions, deletions, and duplications. Repeat masking of insertions, deletions, and
217 duplications with Repbase CENSOR revealed no evidence of transposition events between
218 serial isolates. Relative to the genome reference strain H99, all three case 15 isolates contain a
219 segmental duplication of ~614 kb of the left arm of chromosome 5 and a translocation between
220 chromosomes 4 and 14 where the breakpoint lies in the predicted centromeres (Fig 2D).
221 Rearrangements that occurred between serial isolates include an inversion of ~1.26 Mb on
222 chromosome 3 in the relapse and relapse 2 isolates and a translocation between chromosomes
223 1 and 9 in the relapse 2 isolate (Fig 2D). Breakpoints for both inter-isolate rearrangements were
224 outside of the predicted centromeres. No TE annotations were observed near rearrangement

225 breakpoints, suggesting that another source of sequence homology or homology-independent
226 DNA repair mechanisms mediated these rearrangements.

227 To further characterize the active DNA transposon CNIRT6, we performed sequence
228 analysis and found that this element was ~7.5 kb in length and contained 24 bp terminal
229 inverted repeats beginning with 'CACTG' (Fig 1C, Table S2). Though no CNIRT6 movement has
230 been reported in the H99 reference strain, a BLAT search revealed two approximately full-length
231 copies in H99 (identity ≥ 90% and coverage ≥ 95%), containing a ~6.9 kb gene annotation
232 (CNAG_01367). Repeat masking of the predicted protein sequence with Repbase CENSOR
233 revealed hits to transposases from TEs in the CACTA and EnSpm superfamilies, which contain
234 a 'CACTA' motif at their distal ends, resembling the 'CACTG' motif found in CNIRT6 (51). To
235 confirm that CNAG_01367 encodes a transposase and refine this classification, a multiple
236 sequence alignment was performed using the amino acid sequences from CNAG_01367 and
237 transposases from several "cut-and-paste" DNA transposons from the CMC (CACTA, Mirage,
238 Chapaev) supergroup (52). This alignment revealed a conserved DDE motif, which catalyzes
239 the "cut-and-paste" mechanism of transposition, indicating that CNIRT6 represents a full-length
240 element predicted to encode a transposase of the CMC superfamily (Fig S3A). To examine the
241 relationship of CNIRT6 to other CMC transposons, an unrooted tree was constructed using
242 transposase amino acid sequences representative of CMC/EnSpm families from animals,
243 plants, and fungi. CNIRT6 formed a statistically-supported clade (Bootstrap value 79%) with
244 CACTA (also known as EnSpm) elements previously identified in other fungi, as well as plants
245 and animals (Fig S3B). We conclude that CNIRT6 is a member of the CACTA superfamily within
246 the CMC supergroup (52).

247 Lastly, given the robust activity of CNIRT6 in case 15 isolates grown in YPAD, we
248 hypothesized that CNIRT6 may have mobilized during recurrent infections associated with other
249 cases. To test this, we performed Southern blots on a subset of cases to identify putative
250 transposition events between incident and relapse isolates. We generated a 551 bp CNIRT6-
251 specific probe and utilized a restriction enzyme that cuts once within CNIRT6, outside of the
252 probe site, and produces a range of fragment lengths separable by gel electrophoresis (Fig
253 S4A). Consistent with whole-genome assembly comparisons, there was no difference in the
254 hybridization band pattern for CNIRT6 among case 15 isolates (Fig S4B). However, several
255 other patient cases displayed differences in CNIRT6 hybridization band patterns among serial
256 isolates (Fig S4B). Case 1 was of particular interest, as it exhibited changes in the molecular

weight of three bands, suggesting that these copies may occupy different genomic locations and indicating putative CNIRT6 transposition events between the incident and relapse isolates.

To investigate putative CNIRT6 transposition events in case 1 isolates, we generated whole-genome assemblies of the incident and relapse isolates and performed BLAT searches using full-length CNIRT6 as the query sequence. No full-length copies of CNIRT6 were detected in either genome; an identical number of truncated copies were present at the same genomic locations in both case 1 isolates (Fig S4C). Additionally, repeat masking of insertions, deletions, and duplications identified by SyRI revealed no evidence of TE mobilization events between the isolates. We conclude that the observed differences in Southern hybridization band patterns likely result from other genomic polymorphisms between the isolates, such as other genomic rearrangements or mutations introducing restriction site polymorphisms, highlighting a limitation of this approach in detecting transposition events. In the case 1 relapse isolate, for example, a translocation was detected between chromosomes 3 and 10, with the breakpoint located outside of the predicted centromere regions. There were no TEs near the breakpoint, suggesting that this rearrangement was not mediated by TE-derived sequence homology.

CNEST transposition drives increased drug resistance rates at 37°C in case 77

For case 77, the relapse, and relapse 2 isolates displayed significant increases in rap+FK506 drug resistance rates during growth at 37°C vs 30°C (Fig 3A). Of mutations in *FRR1* observed after growth at 37°C, 29 – 82% were caused by insertion of a novel DNA transposon, which we named CNEST (*Cryptococcus neoformans* EnSpm-like Transposon; naming rationale described below) (Fig 3B). CNEST insertions appeared identical in length by gel electrophoresis and mapped to introns and exons in *FRR1* (Fig S1B, S5A). Insertions resulted in 2 bp 'TA' TSDs (Fig S5B). CNEST insertion rates were significantly higher for all isolates at 37°C; 22-, 83-, and 36-fold in the incident, relapse, and relapse 2, respectively (Fig 3C). The full-length CNEST sequence obtained by linear amplicon sequencing was ~7.2 kb in length, with 33 bp TIRs beginning with 'CACGG' (Fig 1C, Table S2).

Interestingly, we also identified insertions of the DNA transposon KDZ1, recently characterized by Huang et al. 2024, which occurred at a lower frequency and only during growth at 30°C (Fig 3B) (32). KDZ1 is an ~11 kb element with 241 bp TIRs, and its insertion into *FRR1* resulted in 8 bp TSDs (Fig S5B, Table S2). The KDZ1 putative transposase contains a catalytic core affiliated with the Kyakuja-Dileera-Zisupton (KDZ) superfamily and a predicted Zn-chelating CxC1 domain, both of which have been previously described in fungi (Fig 1C) (53).

Assemblies of the relapse and relapse 2 isolates revealed conserved copy number and position of CNEST and KDZ1 by BLAT analysis (identity ≥ 90% and coverage ≥ 95%) with 4 full-length copies of CNEST and 5 full-length copies of KDZ1 (Fig 3D). No DNA methylation was detected in any CNEST copies, as indicated by methylation frequencies < 0.75 at each CpG site from long-read signal data (Table S4). For KDZ1, a single copy contained one methylated CpG in the relapse (Table S4). In the relapse 2, two KDZ1 copies contained one methylated CpG. The additional methylated CpG in the relapse 2 isolate is ~900 bp upstream of the predicted transposase start codon; however, a single methylated CpG seems unlikely to impact transcription of the transposase.

No major genomic rearrangements were identified between the relapse and relapse 2 assemblies. Additionally, no other TE-mediated genomic changes were detected, as all insertions, deletions, and duplications identified by SyRI were repeat masked and showed no significant sequence similarity to TEs in the Repbase library. Although mutation rate and spectra data are provided for the case 77 incident isolate, there was some variability in the growth of independent colonies and some inconsistency in mutation rate observed between independent fluctuation assays. The likelihood of genome instability in this isolate led to its exclusion from nanopore sequencing and genome assembly.

To further characterize CNEST, which has not previously been identified as mobilizing in the H99 reference strain, we performed a BLAT homology search, which revealed two approximately full-length copies in H99 (≥ 90% identity and ≥ 95% coverage), containing a ~4.4 kb gene annotation (CNAG_05910). Repeat masking of CNEST and the predicted amino acid sequence of CNAG_05910 revealed no hits to TEs or transposases in the Repbase library. However, given the identification of CNIRT6 as a member of the CMC supergroup, we predicted that CNEST may also encode a CMC transposase. Multiple sequence alignment of the CNAG_05910 amino acid sequence with transposases of the CMC supergroup revealed a well-conserved DDE catalytic core, confirming CNAG_05910 as a CMC-type transposase encoded within full-length CNEST (Fig S3A). Phylogenetic analysis places CNEST in a distinct clade from CNIRT6, forming part of a strongly-supported clade (Bootstrap value 100%) containing unclassified transposases from diverse animals, including a transposase annotated as an EnSpm/CACTA element in the Pacific oyster (*Crassostrea virginica*) (Fig S3B). This clade is sister to clades of elements containing Chapaev and Mirage transposases from animals, forming a well-supported monophyletic group (Bootstrap value 86%) (Fig S3B). Thus, CNEST encodes a transposase defining a new superfamily within the CMC supergroup that is distinct

322 but most closely related to Chapaev and Mirage superfamilies. In summary, two elements
323 mobilized to mediate drug resistance in case 77: KDZ1, which was detected only at 30°C, and
324 CNEST, which mobilized significantly more frequently at 37°C and is now characterized as a
325 novel active TE in *C. neoformans* belonging to the CMC supergroup. Note that the KDZ
326 superfamily, to which KDZ1 belongs, is completely distinct from the CMC supergroup, which
327 includes CNEST and CNIRT6.

328 **Diverse TEs drive temperature and strain-specific TE mobilization dynamics in case 7**

329 The case 7 incident isolate displayed a significantly higher rap+FK506 resistance rate
330 following growth at 37°C compared to 30°C, while the relapse isolate showed no significant
331 difference in drug resistance rates (Fig 4A). For the incident and relapse isolates at 37°C, ~30%
332 of mutations in *FRR1* were caused by insertions of the LTR retrotransposon TCN3, with both
333 full-length and solo LTR insertions detected (Fig 4B, Fig S1C). TCN3 is ~6.3 kb in length with
334 606 bp LTRs, and insertion into *FRR1* occurred in introns and exons, resulting in 5 bp TSDs of
335 variable sequence (Fig 1C, Fig S6A, B, Table S2). TCN3 is a member of the Ty3/gypsy
336 superfamily that has been previously characterized (54). The TCN3 insertion we identified
337 contains a ~4.7 kb open reading frame with apparently intact Pol domains (reverse
338 transcriptase, RNase H, protease, and integrase) (Fig 1C). Although we did not identify a Gag
339 domain, the first 306 amino acids lack recognizable functional domains and correspond to the
340 region that typically encodes Gag in Ty3/gypsy elements (54). Moreover, the Gag gene is the
341 most variable component of LTR retrotransposons, making it particularly difficult to detect (55).
342 These observations suggest that TCN3 likely represents an autonomous LTR retrotransposon
343 (Fig 1C, Table S2). We recovered no TCN3 insertions at 30°C out of a total of 68 independent
344 mutants screened, suggesting that the element may exclusively mobilize at higher temperatures
345 (Fig 4B).

346 Surprisingly, over 60% of *FRR1* mutations in the case 7 relapse isolate at 30°C were caused
347 by insertions of diverse TEs, including the non-LTR retrotransposon CNL1 and the DNA
348 transposons KDZ2 and KDZ3 (Fig 4B, Fig S1C). In contrast, mutations in the incident isolate at
349 30°C were exclusively SNPs/indels (Fig 4B). The longest CNL1 insertion we identified in *FRR1*
350 was ~3.5 kb in length and contained a ~2.5 kb open reading frame with an apparently intact
351 reverse transcriptase domain (Fig 1C, Fig S1C). This maximum insertion length matches
352 previous reports of CNL1 transposition (38). CNL1 insertions identified in *FRR1* ranged from
353 180 bp to ~3.5 kb likely due to premature termination of reverse transcription which can occur
354 during target primed reverse transcription (TPRT) (56). CNL1 insertions occurred in the *FRR1* 5′

355 untranslated region (UTR) and in an exon, and were associated with TSDs of variable length (0
356 – 13 bp), consistent with findings from prior studies (Fig S6A, B) (38). For KDZ2 (~9.2 kb with
357 139 bp TIRs) and KDZ3 (~10 kb with 169 bp TIRs), insertion into *FRR1* occurred in introns and
358 exons and resulted in 4 – 8 bp TSDs (Fig 1C, Fig S6A, B, Table S2). The internal sequences of
359 KDZ2 and KDZ3 encode putative transposases with KDZ and CxC1 domains (Fig 1C). Although
360 TCN3 and KDZ3 were previously annotated, this study is the first to demonstrate their mobility.

361 BLAT analysis of case 7 genome assemblies using full-length TE sequences that inserted
362 into *FRR1* as queries revealed conserved copy number and position of full-length TCN3 (2
363 copies), KDZ2 (2 copies), and KDZ3 (3 copies) between the incident and relapse isolates (Fig
364 4C). This indicated that the observed KDZ2 and KDZ3 activity in the relapse isolate was not due
365 to an increase in copy number or change in genomic position. Additionally, no DNA methylation
366 was detected on any full-length KDZ2 or KDZ3 copies in case 7 isolates, and no TE sequence
367 polymorphisms were observed between serial isolates (Table S4). We did, however, identify an
368 expansion of CNL1 copies in the relapse isolate, with the number increasing from 16 to 39 full-
369 length copies in arrays in the subtelomeres (Fig 4C). CNL1 copies exhibited varying levels of
370 DNA methylation (Fig 4C, Table S4). The expansion in CNL1 copy number may explain the
371 observed CNL1 mobility in the relapse isolate, which was undetected in the incident isolate (Fig
372 4B). No genomic rearrangements or other TE-mediated changes, including alterations in copy
373 number or position of TCN3 solo LTRs, were identified between the case 7 isolates.

374 Interestingly, we recovered 13 total CNL1 insertions in *FRR1*; however, all full-length CNL1
375 copies in case 7 genome assemblies are located at the ends of incident and relapse
376 chromosome arms, flanked externally by telomeric repeats (“TAACCCCC,” or slight variations
377 thereof), consistent with previous reports (Fig 4C (19,57). To further characterize CNL1, we
378 performed a phylogenetic analysis of the full-length CNL1 insertion in *FRR1* and the CNL1
379 consensus sequence from Repbase. This analysis revealed that CNL1 is more closely related to
380 non-LTR elements of the R2 superfamily (Fig S3C), which are characterized by a single open
381 reading frame and often insert into specific target sequences (58,59), in contrast to other non-
382 LTR retrotransposons such as LINE1 elements which have weak target site specificity (60,61).
383 CNL1 was found to be most closely related to a telomeric-targeting element, MoTeR, described
384 in the fungal plant pathogen *Magnaporthe oryzae* (Bootstrap value 100%) (62). Prior studies of
385 CNL1 insertions reported that over 70% occurred within other CNL1 copies, but found no strict
386 sequence specificity at insertion sites (19), despite CNL1’s close relationship to sequence-
387 specific elements like MoTeR of the R2 superfamily. However, we did observe similarity in the

388 TSDs between independent CNL1 insertions, suggesting potential sequence-specific target site
389 preferences (Fig S6A, B).

390 Centromeres in *C. neoformans* are typically enriched for LTR retrotransposons with > 95%
391 of LTR retrotransposons, including TCN3, restricted to centromeric regions in the H99 genome
392 reference strain, though the mechanism or selective pressure driving centromere targeting of
393 insertions remains unclear (39). Although endogenous TCN3 copies in case 7 isolates are
394 restricted to centromeres, 68 independent TCN3 insertions were detected in *FRR1* (Fig 4B).
395 Mapped insertions occurred at variable sequences and positions within *FRR1*, indicating a lack
396 of strong sequence-specific insertion preference (Fig S6A, B).

397 *C. neoformans* centromeres are also enriched for DNA methylation, which is thought to
398 contribute to repression of TEs present in these regions (40,41). Therefore, we assessed
399 whether the centromeric copies of TCN3 were methylated. If methylated, demethylation and
400 subsequent derepression of TCN3 under heat stress in vitro might explain the observed TCN3
401 mobility at 37°C in case 7 isolates (63). We found that the full-length copies of TCN3 in the case
402 7 isolate genomes reside in hypomethylated regions within the predicted centromere region of
403 Chr 3 for the incident and relapse (data for the relapse isolate not shown) (Fig 4D). While five to
404 seven 5mC DNA methylation marks were observed in full-length TCN3 copies, they are located
405 at the end of the 3' LTR (Fig 4D, Table S4). This region is not typically transcribed, making the
406 observed DNA methylation unlikely to impact TCN3 transposition (64). This suggests that loss of
407 DNA methylation at full-length TCN3 copies is unlikely to underlie the differential activity of
408 TCN3 observed in vitro, where transposition occurred only at 37°C.

409 Our group previously identified the LTR-retrotransposon TCN12 in *Cryptococcus*
410 *deneoformans* as heat stress-activated, mobilizing almost exclusively at 37°C (30,31). In *C.*
411 *neoformans*, heat shock binding elements (HSEs) in the promoter region of heat-responsive
412 genes have been shown to be bound by the transcriptional activator heat shock factor 1 (Hsf1)
413 during heat stress (65). A putative HSE was previously identified in the Tcn12 LTR (31), and
414 upon scanning the TCN3 LTR, we identified two putative HSEs (Fig 4E). This suggests that the
415 elevated mobilization rates of TCN3 and TCN12 at 37°C may result from Hsf1 binding and
416 subsequent upregulation, a hypothesis that our group is currently investigating (65).

417 **Limited nutrient availability alters TE activity**

418 To better mimic the limited nutrient availability *C. neoformans* experiences in-host and
419 assess impacts on TE activity, we compiled the spectra of mutations in the *FRR1* reporter gene

420 for case 7, 15, and 77 following growth in chemically defined RPMI tissue culture medium at
421 37°C (66). The medium was supplemented with less glucose (0.2%) compared to YPAD (2%)
422 and had a defined starting pH of 7.0. For five of the six isolates, the same TEs were identified as
423 mobile in YPAD and RPMI medium (Fig S7A, B, C). However, the proportion of TE-mediated
424 insertions during growth in RPMI decreased compared to growth in YPAD at 37°C (Fig S7A, B,
425 C, Fig 2B, Fig 3B, Fig 4B). This indicates that the additional stressor of nutrient limitation may
426 act to suppress TE mobilization in some instances. One exception was the case 15 incident
427 isolate which displayed comparable TE mutation spectra in both growth conditions (Fig S7A, Fig
428 2B). Additionally, in the case 77 incident isolate, CNL1 was identified inserting into *FRR1*, which
429 had not been previously observed in experiments using YPAD medium (Fig S7B).

430 We additionally tested the impact of RPMI medium at 30°C for case 7 isolates given the
431 activity of CNL1, KDZ2, and KDZ3 observed in the relapse isolate at 30°C in YPAD medium (Fig
432 4B). Interestingly, the use of RPMI medium altered TE dynamics in an isolate- and temperature-
433 specific manner in case 7 isolates (Fig S7C). Differences between YPAD and RPMI medium
434 include: (1) no TCN3 insertions observed in the relapse at 37°C, (2) KDZ3 insertions caused
435 ~35% of mutations in the incident at 30°C, which were absent in YPAD, and (3) variations in the
436 proportion of CNL1, KDZ2, and KDZ3 insertions at 30°C and 37°C in the relapse, highlighting
437 the complex relationship between environment, genetic background and TE activity in case 7
438 isolates.

439 **CNEST heat stress-activation is conserved in a geographically and temporally distinct**
440 **environmental isolate**

441 BLAT analysis revealed full-length CNEST and KDZ1 copies in a previously published *C.*
442 *neoformans* genome, sequenced from an environmental isolate collected from cockatoo
443 droppings in Boston in 2000 (designated cockatoo guano isolate) (26,67). To better understand
444 mobility of CNEST and KDZ1 in a different strain background, we assessed rap+FK506 drug
445 resistance rates and the spectra of mutations in *FRR1*. Indeed, cockatoo guano isolate drug
446 resistance rates were significantly elevated during growth at 37°C compared to 30°C (Fig 5A).
447 Approximately 20% of mutations in *FRR1* at 37°C were CNEST insertions, while no CNEST
448 insertions were observed at 30°C, strongly supporting that CNEST transposition is induced by
449 heat stress in the cockatoo guano isolate (Fig 5B). The cockatoo guano and case 77 isolates
450 both belong to the VNII clade and are geographically and temporally distinct, as the case 77
451 isolates were collected eight years later in South Africa. To assess the copy number and
452 genomic context of CNEST and KDZ1, we performed BLAT searches and synteny analysis

453 using SyRI, which demonstrated that both the copy number and genomic position of CNEST
454 and KDZ1 were conserved (Fig 5C). This may suggest that mobilization of CNEST and KDZ1 in
455 the VNII lineage is infrequent, that mobilization events are typically detrimental to fitness, or that
456 there is selective pressure to maintain both the copy number and genomic context of these
457 elements.

458 A recent study performed two rounds of passaging the cockatoo guano isolate through
459 A/J mice via retro-orbital intravenous injection, collecting isolates from the brain and lungs
460 following each passage (26). Additionally, the cockatoo guano isolate was the point-source
461 isolate for a case of cryptococcal meningitis, from which a single isolate was collected from the
462 patient (PU isolate) (67). To assess whether transposition of CNEST or KDZ1 occurred during
463 murine passage or human infection, Southern analysis was performed using 551 bp CNEST-
464 and 567 bp KDZ1-specific probes, along with restriction enzymes that cut once within the TE
465 sequence, outside of the probe site, to produce a range of fragment lengths (Fig S8A). The
466 same hybridization band patterns were observed in the original cockatoo guano isolate and in
467 all isolates recovered following infection (Fig S8B, C), indicating that no CNEST or KDZ1
468 mobilization occurred during infection, despite detection of CNEST transposition in vitro at 37°C
469 (Fig 5B). Thus, while heat-stress activation of CNEST appears conserved between
470 environmental and clinical isolates, no transposition events were detected in serial isolates
471 recovered from human or murine infections.

472 **Full-length copies of TEs are present across multiple isolates and lineages**

473 Because TE mobility was highly isolate- and strain-dependent in the case 15, 77, and 7
474 isolates, where the TEs captured mobilizing were unique to each case, we hypothesized that
475 this may be due to the absence of full-length copies in certain isolate backgrounds. To evaluate
476 the prevalence of full-length TE copies across *C. neoformans* isolates, we conducted homology
477 searches in assembled genomes using the active TE sequences that were identified inserting
478 into the *FRR1* gene as queries. Full-length copies were defined as hits with ≥ 90% nucleotide
479 identity and ≥ 95% coverage of the query sequence. We identified full-length copies of CNIRT6,
480 CNEST, TCN3, KDZ1, and KDZ3 in several genomes of isolates where transposition was not
481 detected using the *FRR1* reporter screen. We did not, however, identify full-length copies of
482 KDZ2 or CNL1 in other isolates; these elements were present only in those where transposition
483 occurred (Fig S9A). For example, at least one full-length copy of CNEST was found in all
484 genomes assessed, including strains from the VNI, VNII, and VNBII lineages (Fig S9A).

485 To assess whether full-length copies were present in the 15 *C. neoformans* cases initially
486 screened without available whole-genome assemblies, we performed TE copy number
487 estimation by aligning short reads to TE sequences and estimating copy number based on
488 normalized read depth (defined as the depth at which ≥ 95% of the TE sequence is covered)
489 (32). This analysis revealed that full-length copies of potentially active elements were likely
490 present even in isolates in which no TE mobilization was detected in the initial screen, including
491 cases where estimated copy numbers exceeded those in isolates with observed mobilization
492 (Fig S9B).

493 **DNA methylation status may explain differential mobility of TCN3**

494 Although each TE identified in this study was detected mobilizing exclusively in a single
495 isolate background, with the exception of CNEST and CNL1, additional full-length copies were
496 found in other assemblies or inferred through copy number estimation (Fig S9A, B). This
497 suggests that TE activity may be differentially regulated across isolate backgrounds. For
498 example, elevated TE mobility in some isolates may be explained by a loss of RNAi functionality
499 or the absence of DNA methylation on TE sequences.

500 To explore potential regulatory mechanisms, we first assessed the levels of DNA
501 methylation in full-length TE copies in which mobilization was either observed or not observed
502 using the *FRR1* reporter gene. Full-length TCN3 copies were highly methylated in cases 15 and
503 1, whereas hypomethylated copies were observed in case 7 isolates (Table S4). In contrast,
504 DNA methylation was generally absent from full-length DNA transposons in strains where no
505 mobilization was observed. For example, in whole-genome assemblies, full-length KDZ1, KDZ3,
506 and CNEST elements were unmethylated in isolates where transposition was not observed in
507 *FRR1*, with the exception of CNEST in case 1 (Table S4). These findings suggest that while
508 DNA methylation may play a role in regulating TCN3 mobility at the centromeres, the
509 methylation status of full-length DNA transposons (which are primarily unmethylated) does not
510 explain isolate- or strain-specific differences in mobility.

511 Next, we examined whether genes required for RNAi function were intact in cases where
512 TE mobility was observed. In cases 7, 15, 77, and the cockatoo guano isolate, we screened for
513 predicted loss-of-function mutations (defined as predicted protein sequences < 85% of the
514 expected length) using a previously published list of genes essential for RNAi (32). No genes
515 required for RNAi function exhibited truncated protein sequences, providing no evidence for
516 loss-of-function mutations. However, it is possible that nonsynonymous changes could also

517 render RNAi ineffective, which is a limitation of this approach. Alternatively, differential targeting
518 by RNAi or the accumulation of point mutations in TEs may have rendered some full-length
519 copies incapable of transposition.

520 **DNA transposons are predominantly unmethylated and commonly found in gene-rich**
521 **regions**

522 We observed that all full-length, active DNA transposons mapped in the case 15, 77, and
523 7 genomes were located in gene-rich regions along the chromosome arms (Fig 2D, 3D, 4C).
524 Previous studies have highlighted distribution biases of LTR and non-LTR retrotransposons in
525 *Cryptococcus*, with LTR elements predominantly localized in centromeres (39), and non-LTR
526 elements enriched at chromosome ends (38). To further investigate the genomic distribution of
527 DNA transposons in *C. neoformans*, which has not previously been described, we took a
528 comprehensive, unbiased approach to assess genome-wide TE content and distribution. De
529 novo TE annotation was performed using the Earl Grey package (68) for cases 1, 7, 15, and 77,
530 as well as the genome of the reference strain H99, in which TE mobilization has not been
531 observed unless RNA interference (RNAi) is disrupted (36,38). Results from the first assemblies
532 of serially collected isolates are shown, as assemblies of later relapse isolates from the same
533 patients yielded similar results. TEs occupied approximately 3 – 5% of the genomes analyzed
534 (Fig 6A). While the proportion of LTR-retrotransposons remained relatively consistent (2.2 –
535 2.6%), greater (more than tenfold) variation was observed in the proportion of DNA transposons
536 (0.08 – 0.85%), and non-LTR retrotransposons (0.06 – 2.06%) (Fig 6A). Notably, the *C.*
537 *neoformans* reference strain H99 had the lowest proportion of DNA transposons among all
538 isolates analyzed.

539 To visualize TE distributions, chromosomes were split at the midpoint of the predicted
540 centromere. For each chromosome arm, the length, TE positions, and protein-coding gene
541 annotation positions were scaled from 0 to 1, allowing data from all chromosome arms to be
542 plotted on a single track. In agreement with previously published data, LTR and non-LTR
543 elements cluster in the predicted centromeres and subtelomeres, respectively; these are
544 regions with a lower density of protein-coding genes (Fig 6B). By contrast, DNA transposons
545 appear to be more evenly distributed across chromosome arms (Fig 6B). We used quantile-
546 quantile (QQ) plots to assess whether the positions of DNA transposons along chromosome
547 arms follow a uniform distribution. For each genome, we generated theoretical quantiles as
548 sorted random numbers between 0 and 1; the total number of theoretical quantiles matched the
549 total number of DNA transposons. The plotted points fell approximately along the diagonal of the

550 QQ plots, indicating that DNA transposons were distributed roughly uniformly across the
551 genome (Fig S10).

552 To assess how frequently DNA transposons were methylated, given their presence in
553 gene-rich regions that are not typically methylated in *C. neoformans* (41,42), we compared their
554 5-methylcytosine (5mC) DNA methylation levels to those of LTR and non-LTR elements. First,
555 we assessed average methylation density per 100 bp. DNA transposons exhibited significantly
556 lower average 5mC densities compared to both non-LTR and LTR retrotransposons (pairwise
557 Wilcoxon rank-sum test with continuity correction; adjusted *p* values < 2e-16 for both
558 comparisons) (Fig 6C). Additionally, LTR elements exhibited significantly higher DNA
559 methylation densities compared to non-LTR elements (pairwise Wilcoxon rank-sum test with
560 continuity correction; adjusted *p* value < 2e-16). Second, we assessed the proportion of TE
561 annotations per genome containing at least one high-confidence 5mC call (methylated
562 frequency from nanopore long-read signal data > 0.75). According to this analysis, we found
563 that LTR elements are by far the most consistently methylated (55.6 – 71.2% of LTR
564 retrotransposons contained at least one predicted 5mC), followed by non-LTR elements (7.7 –
565 53.4%), and DNA transposons (5.4 – 15.5%) (Fig S11A, B). The number of methylated LTR and
566 non-LTR retrotransposons was significantly enriched compared to DNA transposons (Fisher's
567 method combined *p* values: 3.2e-64 for LTR elements and 9.2e-19 for non-LTR elements).

568 To estimate background levels of DNA methylation in protein-coding genes, we lifted
569 over gene annotations from the H99 reference genome. The percentage of protein-coding
570 genes with at least one high-confidence 5mC call ranged from 0.5 – 4.5%, indicating that DNA
571 TEs remain significantly enriched for DNA methylation relative to endogenous protein-coding
572 genes (Fisher's method combined *p* value 3.9e-10), albeit at a lower frequency than LTR and
573 non-LTR elements. Thus, the majority of DNA transposons across all genomes analyzed are
574 unmethylated, and those that are methylated exhibit a lower methylation density compared to
575 non-LTR and LTR retrotransposons (Fig 6C, Fig S11A, B). This suggests that DNA methylation
576 is unlikely to play a major role in modulating the activity of DNA transposons in *C. neoformans*.

577

578 **DISCUSSION**

579 Understanding the interplay between mobile genetic elements, environmental stressors,
580 epigenetics, and genetic background is critical for uncovering factors that influence evolutionary
581 rates and the capacity for adaptive change, particularly in the context of fungal pathogens. In

582 this study, we screened a collection of clinical *Cryptococcus* isolates for transposable element
583 (TE) insertions in the *FRR1* reporter gene and profiled rates of rapamycin and FK506
584 (rap+FK506) resistance, as well as mutation spectra, at both 30°C and the heat-stress condition
585 of 37°C. We also generated telomere-to-telomere genome assemblies to assess TE copy
586 number, genomic position, and DNA methylation status in isolates from patients with recurrent
587 cryptococcal infections.

588 ***C. neoformans* hosts diverse active transposable elements**

589 We identified seven TE families mobilizing to confer rap+FK506 resistance, including
590 both class I retrotransposons (LTR and non-LTR) and class II DNA transposons (Fig 1). Several
591 of these elements, such as TCN3, CNIRT6, and KDZ3, were not previously recognized as
592 active. In addition, we discovered a novel, active, and previously uncharacterized element,
593 which we named CNEST. The diversity of active TEs in *C. neoformans* stands in striking
594 contrast to other yeasts commonly used to study TEs, such as *Saccharomyces cerevisiae* and
595 *Schizosaccharomyces pombe*, which harbor only LTR retrotransposons (69,70). In these
596 species, TE mobilization studies typically rely on reporter constructs driven by inducible
597 heterologous promoters, due in part to the low de novo transposition rates of endogenous TEs
598 (71–74). By contrast, in *C. neoformans*, screening for mutations at a single genomic locus using
599 a 'transposon trap assay' frequently revealed insertions of endogenous TE copies with diverse
600 transposition mechanisms (Figs 2 – 5). The ability to readily capture multiple active TE families
601 mobilizing within a single *C. neoformans* strain underscores the potential for utilizing forward
602 mutation reporters as a powerful, genetically tractable model for studying TE mobilization
603 strategies and regulation.

604 Phylogenetic analysis of transposases from the DNA transposons CNIRT6 and CNEST
605 revealed that they belong to the CMC supergroup first described by Yuan and Wessler (2011)
606 (Fig S3). This supergroup includes EnSpm, one of the two transposon systems originally
607 discovered in maize by Barbara McClintock (51,75). However, CNIRT6 and CNEST are only
608 distantly related and fall within two monophyletic clades among CMC elements: one containing
609 CNIRT6 and transposase sequences from plants, animals, and fungi, and a second containing
610 CNEST and transposases from animals and fungi. Thus, *C. neoformans* hosts active members
611 of two different CMC superfamilies, a notable finding given that this group of DNA transposons
612 remains largely understudied in fungi and animals. CNEST and CNIRT6 offer an opportunity to
613 study two distinct active CMC transposons in a model fungal species.

614 Notably, the use of a single reporter gene to capture TE insertions may have limited our
615 potential for active mobile element discovery, since some TEs have preferences for specific
616 insertion sequences or genetic compartments (10). However, the *FRR1* reporter system
617 recovered insertions of TCN3 and CNL1, which appear to target centromeric and subtelomeric
618 regions, respectively. TCN3 insertions in *FRR1* occurred at multiple positions and were
619 associated with variable terminal site duplications (TSDs), suggesting weak sequence specificity
620 (Fig S6). Alternatively, TCN3 may recognize non-sequence-based features of centromeres, such
621 as centromere-specific histone variants (79) or heterochromatin-associated proteins (80), or its
622 insertion pattern may be shaped by selective pressures. Since our approach captures insertions
623 only at the *FRR1* locus, we cannot assess genome-wide insertion preferences. It remains
624 possible that insertion into *FRR1* is relatively rare and that most de novo TCN3 insertions occur
625 within centromeric regions, warranting further investigation in future studies.

626 CNL1 copies are enriched in subtelomeric regions in case 7 isolates and other *C.*
627 *neoformans* genomes (38); however, we also recovered insertions of CNL1 within *FRR1* (Fig 4).
628 Phylogenetic analysis revealed that CNL1 is most closely related to R2 elements, and
629 specifically to MoTeR, a telomere-targeting element characterized in the fungal plant pathogen
630 *Magnaporthe oryzae* (62). Although prior studies have reported that CNL1 preferentially inserts
631 into copies of itself within arrays near telomeric repeats, its precise sequence specificity remains
632 undefined. Through limited mapping, we observed two insertion locations for CNL1 within
633 *FRR1*: one in the 5′ UTR and another within an exon (Fig S6). These insertions generated TSDs
634 of variable length, though interpretation was complicated by premature termination of target
635 primed reverse transcription (TPRT) at different positions within the element. Notably, many of
636 the observed TSDs contained the sequence 'CACCCCT,' which resembles the *C. neoformans*
637 telomere seed sequence ('AACCCCCT' or similar variants). Further work is needed to clarify
638 CNL1's target site specificity, including the extent to which it targets telomeric repeats like
639 MoTeR, inserts into its own sequence, or both, and to understand how these insertion
640 preferences contribute to its transposition into *FRR1*. Together with findings from TCN3, these
641 observations highlight important open questions about the factors that govern target site
642 selection and the evolutionary forces shaping TE insertion patterns across genomic
643 compartments. Intriguingly, one such factor may be stress, which has been shown to alter target
644 specificity. For example, Ty5 phosphorylation is regulated by nutrient deprivation stressors,
645 shifting its insertion profile from heterochromatic regions to more broadly distributed sites across
646 the genome (80).

647 Lastly, most observed TE mobilization events were driven by apparently full-length TE
648 copies containing detectable functional domains required for mobilization. Phylogenetic analysis
649 revealed full-length, seemingly intact transposase sequences within mobilized DNA
650 transposons, and functional domains required for mobilization were identified in mobilized TCN3
651 and CNL1. We found no evidence for the mobilization of non-autonomous TE copies
652 (significantly shortened or lacking apparent mobilization machinery). However, we did detect
653 truncated CNL1 insertions, likely resulting from premature termination of reverse transcription,
654 as well as instances of solo TCN3 LTRs, which likely arose from non-allelic recombination
655 between LTR sequences following TCN3 insertion. This contrasts with other organisms, such as
656 humans, plants, and *Drosophila*, where shortened non-autonomous TEs frequently transpose
657 (76–78).

658 Collectively, we identified seven mobilizing TE families: DNA transposons from the KDZ
659 superfamily and CMC supergroup, alongside a Ty3/Gypsy LTR element and an R2 non-LTR
660 element actively transposing in *C. neoformans*. These TEs employ distinct transposition
661 mechanisms and show preferences for different genomic compartments, revealing a rich
662 "ecosystem" of active transposable elements within *C. neoformans*.

663 **Transposable element mobilization in *C. neoformans* is strongly influenced by**
664 **temperature**

665 Previous work in *C. deneoformans* demonstrated that heat stress increases TE
666 mobilization (30,31). Building on this, we screened 15 clinical *C. neoformans* isolates for TE
667 insertions in the *FRR1* reporter gene at 37°C. While some elements followed the pattern
668 previously observed in *C. deneoformans*, mobilizing more frequently at elevated temperature,
669 we also uncovered TEs that behave differently. Several elements (CNL1, KDZ1, KDZ3) were
670 found to mobilize exclusively at 30°C. Others (CNIRT6, CNEST) mobilized at both
671 temperatures, but with higher frequency at 37°C. Therefore, by limiting our initial screen to 37°C
672 and examining only ten independent mutants, we may have overlooked strains harboring mobile
673 elements that are active only at lower temperatures or that mobilize at low frequency.

674 The LTR retrotransposon TCN3 was observed to mobilize exclusively at 37°C (Fig 4),
675 paralleling earlier findings in *C. deneoformans*, where heat stress activated the LTR
676 retrotransposon TCN12, which contains a heat shock element (HSE) in its LTR promoter region
677 (31). In TCN3, we identified two putative HSEs within its LTR, suggesting potential regulation by
678 the heat shock transcription factor Hsf1, a key coordinator of the heat shock response (65).

679 While heat shock-induced TE activation via host machinery has been demonstrated in plants
680 and animals (81–83), this mechanism has not been described in fungi. We are currently testing
681 the hypothesis that TCN3 and TCN12 co-opt the host heat shock response to facilitate their
682 mobilization.

683 Other temperature-dependent effects on TE mobility may be attributed to self-regulatory
684 mechanisms of the TE-encoded machinery or to alteration of TE suppression mechanisms at
685 different temperatures. As an example of the former, Ty1 element mobilization in *S. cerevisiae* is
686 most frequent at 22°C and is not observed at temperatures above 34°C due to inactivity of the
687 Ty1-encoded protease (84). As an example of the latter, in *Drosophila*, heat stress triggers heat
688 shock protein 70 (Hsp70) to displace PIWI-interacting RNA (piRNA) biogenesis factors to the
689 lysosome for degradation, leading to transcriptional activation of TEs (85). In *C. neoformans*, a
690 recent study found a link between the Calcineurin signaling pathway, which is necessary for
691 stress adaptation and growth at 37°C, and RNAi-mediated silencing of a repetitive transgene,
692 suggesting a potential mechanism for altered RNAi function during heat stress (86). Further
693 studies are needed to elucidate the mechanisms underlying differential TE mobilization under
694 heat stress in *C. neoformans*, which will inform our understanding of TE dynamics and their role
695 in adaptive evolution during infection and in other heat-stress contexts.

696 While temperature plays a significant role in driving TE mobilization, additional
697 environmental factors likely contribute as well. Nutrient limitation in RPMI medium altered TE
698 mobilization dynamics across most strains (Fig S7). Moreover, although CNL1 mobilization was
699 only observed in vitro at 30°C, it was the sole TE implicated in genomic changes during
700 recurrent cryptococcal infection, where cells encounter mammalian body temperature. This
701 underscores the complex interplay between environmental conditions and TE activity,
702 highlighting that temperature is not the sole regulator. Other stressors or environmental stimuli
703 may act concurrently to activate or repress TE mobility, although under our in vitro conditions,
704 temperature remains a major regulator of TE mobilization across genetically diverse *C.*
705 *neoformans* strains.

706 **DNA transposons are hypomethylated relative to retrotransposons, and are commonly**
707 **found in gene-rich regions**

708 Given that *C. neoformans* lacks a de novo cytosine DNA methyltransferase, DNA
709 methylation as a TE suppression mechanism is relatively inflexible and unlikely to target newly
710 inserted or unmethylated TE sequences (41). Despite this, a substantial proportion of TEs

711 exhibit DNA methylation: 55.6 – 71.2% of LTR elements and 7.7 – 53.4% of non-LTR elements
712 (Fig S11). In contrast, DNA transposons are less frequently methylated, with only 5.4 – 15.5%
713 showing methylation, and when methylated, they exhibit significantly lower average 5mC
714 density compared to LTR and non-LTR elements (Fig 6). This reduced level of methylation may
715 contribute to the more frequent mobilization of DNA transposons observed in this study, where
716 five of the seven mobile elements identified were DNA TEs. Furthermore, full-length DNA
717 transposons are more evenly distributed across the genome and are commonly found within
718 gene-rich regions, whereas LTR and non-LTR retrotransposons tend to be enriched in gene-
719 poor centromeric and subtelomeric regions. As a result, DNA TEs may be more likely to mediate
720 genetic changes that alter the expression or function of protein-coding genes which could drive
721 adaptation under stress conditions.

722 **Transposable elements provide a mechanism for rapid genetic change and facilitate**
723 **adaptation in *C. neoformans***

724 Growth at mammalian body temperature (37 °C) significantly increased the rate of
725 acquired resistance to rap+FK506 in both clinical and environmental isolates (Figs 2–5). In all
726 cases, this effect was driven by elevated TE insertion rates, highlighting the role of TEs in
727 generating adaptive phenotypes such as antifungal resistance. These findings suggest that in-
728 host conditions or other heat stress contexts may enhance evolvability within *C. neoformans*
729 populations through bursts of rapid TE mobilization.

730 RNA interference (RNAi) is the primary known mechanism for TE suppression in *C.*
731 *neoformans*, and loss of RNAi function is associated with hypermutator phenotypes driven by
732 uncontrolled TE activity (38). However, recent work has shown that this is not always the case,
733 as some isolates with loss-of-function mutations in essential RNAi genes maintain low TE
734 burdens and mutation rates (32). In this study, none of the clinical or environmental isolates
735 profiled for mutation spectra harbored predicted loss-of-function mutations in RNAi pathway
736 genes. Nevertheless, isolates from cases 15 and 77 exhibited rap+FK506 resistance rates at
737 37°C comparable to those observed in hypermutator strains, including the mismatch repair-
738 deficient *msh2Δ* mutant (32,38). This suggests that, in certain strain backgrounds, heat stress
739 alone can be sufficient to induce a hypermutator-like phenotype through increased TE activity,
740 even in strains with a relatively low TE burden (e.g., two full-length copies of CNIRT6 in case 15
741 isolates).

742 When assessing the impact of TEs on in-host microevolution, we observed, in one
743 notable case, an expansion of CNL1 copy number in serial isolates collected from a patient with
744 recurrent cryptococcal meningitis, suggesting a role for TE activity in within-host evolution (Fig
745 4). However, no transposition or TE-mediated genomic changes were detected in other
746 longitudinally sampled clinical isolates or in isolates collected following murine passaging. This
747 may suggest that TE mobilization events are rare in vivo, that TE-mediated changes did not
748 confer a selective in-host growth advantage during infection, or that TE-mediated changes
749 occurred in subpopulations not captured by sampling a single isolate. Previous studies in *C.*
750 *deneoformans* found evidence of transposition occurring during murine infection (30,31). In
751 these cases, however, only drug-resistant isolates were selected for recovery from the mice,
752 requiring that loss-of-function mutations at specific reporter loci had occurred in the recovered
753 isolates. In contrast, there was no selective pressure for evolved drug resistance or other traits
754 during the recovery of patient and mice isolates examined in this study.

755 **Genetic background influences TE mobility**

756 Telomere-to-telomere genome assemblies revealed that the presence of full-length TEs
757 does not reliably predict their mobilization in vitro. For instance, in clonally related case 7
758 isolates, we observed striking differences in KDZ2 and KDZ3 mobilization at 30°C, despite
759 these elements being present at identical copy number and genomic positions, with identical
760 sequences, and lacking DNA methylation in both isolates. Interestingly, of the two single
761 nucleotide polymorphisms (SNPs) previously identified between case 7 isolates, one was an
762 amino acid substitution in *SET5* (CNAG_03890), a predicted protein lysine methyltransferase
763 (24). This suggests that alternative epigenetic regulation may be driving differential mobility, a
764 hypothesis we plan to investigate further. Similarly, unmethylated full-length CNEST copies were
765 identified in all assembled genomes except for case 1; however, mobilization was observed only
766 in the case 77 and cockatoo guano isolates. These observations suggest that isolate- and
767 strain-specific TE activity may be regulated by differential RNAi targeting, alternative
768 suppression mechanisms beyond DNA methylation, or disabling mutations. Future studies are
769 needed to dissect the factors underlying differential TE mobility, which may include TE copy
770 number polymorphisms, sequence variation within TEs, or genetic variation in host factors that
771 control transposition.

772 Altogether, our findings highlight the complex interplay between genetic background,
773 epigenetics, and environmental conditions in governing TE mobilization, with temperature
774 emerging as a major determinant. Further studies should investigate the extent to which stress-

775 induced transposition generates genetic diversity and whether this diversification drives
776 adaptation to infection-relevant stressors and the repeated emergence of antifungal drug
777 resistance in *C. neoformans*.

778

779 **METHODS**

780 **Strains and growth media**

781 The strains used in this study are listed in Table S1. Strains were grown in YPAD
782 medium (1% yeast extract, 2% peptone, 2% dextrose, 0.025% adenine) with 2% agar added for
783 solid media. For nutrient limiting conditions, strains were cultured on RPMI plates containing
784 3.45% MOPS, 0.2% glucose, 2% agar, and 1.04% RPMI 1640 powder (Sigma #R1383).
785 Mutants resistant to rapamycin and FK506 (rap+FK506) were selected for on YPAD plates
786 supplemented with 1 µg/mL rapamycin (LC Laboratories) and 1 µg/mL FK506 (Astellas).

787 **Fluctuation assay and mutation spectra**

788 Cultures were inoculated with independent colonies; each colony was split between a
789 30°C and a 37°C culture and grown for 3 days in 1 mL of liquid YPAD, rotating at either 30°C or
790 37°C. Cells were pelleted, washed, and resuspended in water. Cells were appropriately diluted,
791 plated on solid YPAD medium, and incubated at 30°C for 3 days. Colony counts were used to
792 calculate colony forming units (CFUs) per culture. The remainder of the culture was plated on
793 two rap+FK506 plates and incubated at 37°C for four days before counting colonies. Total CFUs
794 and rap+FK506-resistant colony counts were used to calculate mutation rates using the
795 Fluctuation AnaLysis CalculatOR (FALCOR), applying the Ma-Sandri-Sarkar (MSS) Maximum
796 Likelihood Method (87). A single rap+FK506-resistant colony from each culture was selected for
797 genomic DNA isolation, performed using either in-house reagents or a MasterPure Yeast DNA
798 Purification Kit (VWR #76081-694).

799 The *FRR1* gene was amplified for Sanger (Azenta) or linear amplicon long-read
800 sequencing (Plasmidsaurus). Amplification of *FRR1* was carried out using a variety of
801 polymerases: MyTaq Mix (Thomas Scientific #C755G91), Apex Taq RED Master Mix (Genesee
802 Scientific #42-138), Platinum SuperFi II PCR Master Mix (ThermoFisher #12368010), Q5 High-
803 Fidelity DNA Polymerase (NEB #M0491S), and LongAmp Taq DNA Polymerase (NEB
804 #M0323S). We often observed “phantom” wild-type–sized secondary bands when amplifying
805 across TEs, which can occur as a PCR artifact when amplifying across long repetitive DNA

806 sequences (88). In these instances, gel extraction using the Zymoclean Gel DNA Recovery Kit
807 (Zymo Research #D4007) was performed on the higher molecular weight bands, which were
808 then sent for sequencing. For TEs identified as inserting into *FRR1*, where the full sequence
809 was obtained by linear amplicon sequencing, junction PCR with primers targeting the internal
810 TE sequence from the same isolate was used to confirm a subset of insertion events. Primers
811 used to amplify *FRR1* and for TE-specific junction PCR are listed in Table S5.

812 Sanger sequencing data were analyzed in SeqMan Ultra 17 or DNASTAR Navigator 17
813 by aligning reads to the wild-type *FRR1* sequence for each isolate. TEs were assigned to
814 families based on the 80-80-80 rule: nucleotide similarity greater than 80%, over more than 80
815 base pairs, covering at least 80% of the recovered sequence length (48). The TE consensus
816 sequence for TCN3 was obtained from Repbase. For TEs lacking family-level consensus
817 sequences, GenBank submissions were used to assign family membership (GenBank
818 accessions: PQ181658 [KDZ1], PQ181660 [KDZ2], and PQ181661 [KDZ3]). CNL1 family
819 membership was called based on sequence similarity to CNL1 mapped by Priest et al. (2022) in
820 Bt65 and Bt81 genome assemblies (BioProject accession PRJNA749953).

821 **RPMI mutation spectra**

822 To generate independent mutants during growth on RPMI medium, a prong-plating
823 procedure was carried out. Single colonies were inoculated in liquid YPAD and grown overnight
824 rotating at 30°C, then cells were washed and diluted in water. A custom tool containing 121 flat-
825 tipped pins was used to transfer approximately ~10^4 cells/pin onto non-selective RPMI plates
826 (89). To confirm there were no pre-existing mutations, cells were also spotted on rap+FK506
827 plates. Confluent spots of cells on these plates would indicate mutations occurred during the
828 overnight growth in YPAD and prong plating would not be possible to generate independent
829 mutants. If less than 5 colonies appeared on these control plates, experiments were continued.
830 RPMI plates were incubated for 3 days at either 30°C or 37°C. RPMI plates were then replica
831 plated to rap+FK506 plates and incubated at 37° for 3 days. A single colony was picked from
832 each spot for genomic DNA isolation, followed by *FRR1* amplification and either Sanger
833 sequencing (Azenta) or junction PCR. *FRR1* amplification, junction PCR, Sanger sequencing
834 data analysis, and TE classification were carried out as described above.

835 **TE insertion rate**

836 TE insertion rate was calculated using the proportion of independent mutants with a
837 given TE insertion multiplied by the drug resistance rate. The 95% confidence intervals (CI) for

838 proportions were determined using the vassarstats.net proportion CI calculator including
839 continuity correction. 95% CI for TE insertion rates were determined by a method employing the
840 square root of the sum of the squares (using the component 95% CI for rates and proportions)
841 (90).

842 **Transposase and reverse transcriptase protein sequence alignments and phylogenies**

843 Transposase and reverse transcriptase protein sequences were obtained from Yuan and
844 Wessler (2011) for CMC (CACTA, Mirage, Chapaev) related sequences, Repbase consensus
845 sequences (https://www.girinst.org/), and from BLASTp (for translated mRNA sequences) or
846 tBLASTn (for translated genomic sequences) via NCBI (https://blast.ncbi.nlm.nih.gov/Blast.cgi).
847 Protein sequences were aligned using MAFFT (https://www.ebi.ac.uk/jdispatcher/msa/mafft)
848 with the following parameters, protein matrix = BLOSUM62, gap opening penalty = 1.53, gap
849 extension penalty = 0.123, tree rebulding number = 2, max iterations = 2, and FFTS = none.
850 Aligned protein sequences were then used to construct maximum likelihood phylogenies with
851 100 bootstrap replicates using MEGA version 11 (91).

852 **Nanopore sequencing**

853 To extract high molecular weight DNA for library preparation, overnight cultures were
854 grown in 50 mL liquid YPAD shaking at 30°C. Cell were pelleted and lyophilized overnight.
855 Genomic DNA was extracted using a cetyltrimethylammonium bromide (CTAB) extraction
856 method with some modifications (92). Briefly, cells were lysed by bead beating, and DNA
857 extraction buffer (100 mM Tris-HCl, pH 7.5; 1% w/v CTAB; 0.7 M NaCl; 10 mM EDTA; 1% v/v 2-
858 mercaptoethanol) was added and incubated at 65°C for 30 minutes. Chloroform purification was
859 then performed, and layers were separated by centrifugation. The aqueous layer was isolated,
860 and DNA was subsequently precipitated, washed, and treated with RNase A. Sodium acetate
861 (NaOAc) was then added to a final concentration of 0.6 M, and chloroform purification was
862 repeated. DNA was precipitated again, washed, and spooled to collect high molecular weight
863 DNA.

864 DNA quality was assessed using NanoDrop One A260/A280 and A260/A230 ratios
865 (Thermo Fisher Scientific) and quantified using Qubit dsDNA Broad Range Assay Kit (Invitrogen
866 #Q32850) and the Qubit 4 Fluorometer (Invitrogen). To assess DNA fragment length, clamped
867 homogeneous electric field (CHEF) gel electrophoresis was performed using the CHEF Mapper
868 (Bio-Rad). Libraries were prepared using the SQK-LSK110 or SQK-NBD114.24 and EXP-
869 NBD104 kits and sequenced using the MinION Mk1C following manufacturer's instructions

870 (Oxford Nanopore). Sequencing was performed using the MinKNOW software at the default
871 voltage for at least 48 hours. Basecalling was performed using the latest Guppy software
872 (v7.1.4, v6.3.8, or v6.4.8), or with Dorado (v0.8.1). The specific sequencing kit, flow cell, and
873 basecalling methodology used for each isolate are listed in Table S3.

874 **Genome assembly**

875 Demultiplexing was performed using Guppy (v6.5.7). The Canu (v2.2) genome
876 assembler was used to assemble long reads into contigs, small contigs likely representing
877 mtDNA or contaminants (< 200 kb) were discarded (93). For the case 15 incident isolate only,
878 assembly was performed by combining outputs from Canu and Flye (v2.9.5) (94). Genome
879 polishing was performed using long reads generated in this study and short reads available
880 under the SRA umbrella project PRJNA37160 (24). Long reads were mapped to contigs using
881 Minimap2 (v2.24) followed by Medaka (v1.5.0 or v2.0.1) polishing using the appropriate model
882 (95). Short reads were mapped to the draft assembly using Bowtie2 (v2.4.4) followed by Pilon
883 (v1.24) polishing, which was performed in five iterations, re-mapping the short reads to each
884 new draft assembly before the next iteration of polishing (96,97). Canu-corrected Nanopore
885 reads were mapped to the assembly using Minimap2 (v2.24) and coverage was visually
886 inspected in the Integrative Genome Viewer (IGV) (98). To confirm generation of telomere-to-
887 telomere assemblies, contig ends were inspected for the presence of telomere seed sequences
888 (99). Assembly breaks at the rDNA locus were artificially merged and separated by 50 Ns.
889 Contigs were oriented to match the first serially collected isolate assembly to produce final
890 nuclear genome assemblies. For each isolate, Canu parameters, polishing specifications, and
891 assembly statistics are provided in Table S3.

892 **DNA methylation detection**

893 5-methylcytosine (5mC) DNA methylation at CpG sites was called using Nanopolish
894 (v0.14.0) or f5c (v1.5) (see Table S3 for isolate-specific details). Minimap2 (v2.24) was used to
895 map long reads to the final nuclear assembly for each isolate. For DNA methylation detection
896 using f5c, POD5 files were converted to BLOW5 using blue-crab (v0.2.0). The Nanopolish
897 helper script methylation_frequency.py was used to calculate the methylation frequency for CpG
898 sites.

899 **Centromere mapping**

900 Predicted centromere regions were determined using a synteny based approach using
901 the H99 reference genome (GCA_000149245.3) where centromere regions have been
902 experimentally identified (38,39,99). The 5 kb regions flanking H99 centromeres were used as
903 BLASTn (v2.14.0+) queries against assembled genomes for centromere mapping (100,101).

904 **Full-length TE mapping in assembled genomes**

905 To estimate full-length TE copy numbers from assembled genomes BLAT (v35) and
906 BLASTn (v2.14.0+) were used, full-length TE sequences obtained from linear amplicon long-
907 read sequencing of TE insertions into *FRR1* were provided as queries (49). Full-length copies
908 were defined as hits with identity ≥ 90% and alignment length ≥ 95% of the query length. For
909 BLAT the -minIdentity=90 specification was used, and pslReps (v469) filtered hits to find the
910 best alignment with a minimum coverage of 95% (-minCover=0.95). BLASTn hits meeting full-
911 length criteria were filtered in R (v4.3.3). In instances were BLAT and BLASTn reported different
912 full-length copy number estimates, the higher estimate was used. Only BLASTn was used to
913 detect copies of CNL1 because BLAT reported overlapping CNL1 copies leading to
914 overestimation, this was not observed for other TEs.

915 **Identification of structural rearrangements and synteny analysis**

916 Whole-genome alignment was performed using Minimap2 (v2.24). Dotplots to visualize
917 primary alignments between assemblies were generated in R (v4.3.3) using pafr (v0.0.2).
918 Synteny and Rearrangement Identifier (SyRI) (v1.6.3) was used to define syntenic regions and
919 structural rearrangements between serial isolates using default parameters (50). Plotsr was
920 used to visualize syntenic regions (102).

921 **Southern analysis**

922 Genomic DNA was prepared using a CTAB DNA extraction method (described above)
923 and digested with restriction enzymes BspEI, PvuII, or PspXI for CNIRT6, MLDT, and KDZ1,
924 respectively (New England Biolabs) (92). Digests were run on 0.7% agarose gels at 4°C for
925 approximately 16 h. Fragments from the gel were transferred to a charged nylon membrane
926 (Roche). Target probes were prepared using chemiluminescent DIG-labeling (Roche), see Table
927 S5 for primers used to amplify probes. Hybridization of the DIG probes (DIG Easy Hyb
928 Granules, Roche) and detection by chemiluminescence using an anti-DIG antibody (Anti-
929 Digoxigenin-AP Fab Fragments, Roche) were performed according to the recommended
930 manufacturer's protocols and imaged on film (Amersham Hyperfilm ECL).

931 **TE annotation and repeat masking**

932 Transposon annotation was performed using Earl Grey (v4.1.0) with default parameters
933 (68). Repeat masking of insertions, deletions, and duplications identified by SyRI were analyzed
934 using Genetic Information Research Institute (GIRI) Repbase CENSOR (103).

935 **Gene annotation**

936 Gene annotations were lifted over from the H99 reference genome (GCA_000149245.3)
937 by Liftoff (v1.6.3) with the -polish flag (104).

938 **TE copy number estimation using short reads**

939 TE copy number estimation using short reads was performed as previously described
940 (32). Briefly, publicly available short reads (PRJNA37160) were mapped to the H99 reference
941 genome (GCA_000149245.3) using Minimap2 (v2.24), mosdepth (v0.3.10) was used to
942 calculate the median read depth in 500 bp non-overlapping windows, the median depth reported
943 was used for normalization (105). Short reads were also mapped using Minimap2 to a multi-
944 fasta containing all full-length TE sequences identified inserting into *FRR1*. Mosdepth was then
945 used to produce the cumulative read depth distribution. For each TE, read depth at 0.95
946 coverage was normalized by the genome-wide median read depth to estimate full-length copy
947 number.

948 **RNAi gene loss-of-function prediction**

949 Genome feature annotation was "lifted over" from the H99 reference genome (FungiDB
950 R68) to each isolate-specific genome assembly using the software tool Liftoff (v1.6.3) (104). The
951 `-polish` option of Liftoff was employed to re-align exons in cases where the lift-over procedure
952 resulted in start/stop codon loss or introduced an in-frame stop codon. Based on the polished
953 lift-over annotation, the AGAT GTF/GFF Toolkit software (https://github.com/NBISweden/AGAT)
954 was used to predict protein sequences for all annotated genes in each strain-specific assembly
955 using the `agat_sp_extract_sequences.pl` script. Where multiple protein isoforms are annotated
956 in the reference genome, predictions were generated for each isoform. For each RNAi-related
957 gene of interest, the predicted amino acid sequences for each isolate were compared to the
958 H99 reference genome. Candidate loss-of-function alleles were classified as those encoding
959 proteins whose predicted length is < 85% of the length in H99.

960

961 **DATA AVAILABILITY**

962 Raw nanopore sequencing reads and whole-genome assemblies generated from
963 isolates used in this study are available on NCBI's Sequence Read Archive (SRA) under
964 BioProject PRJNA1222431, accession numbers are listed in Table S3. Full-length TE
965 sequences identified inserting into *FRR1* were uploaded to GenBank, accession numbers are
966 listed in Table S2.

967

968 **ACKNOWLEDGEMENTS**

969 We would like to thank Dr. Marco Dias Coelho for training and assistance with de novo
970 genome assembly. Additionally, we thank Dr. Arturo Casadevall for providing the cockatoo
971 guano isolate, as well as the isolates collected after murine passage. This project was
972 conceived and initiated by A. Gusa while a postdoc in the lab of Dr. Sue Jinks-Robertson and
973 was partially supported by National Institutes of Health (NIH) grant R35GM118077 to S. Jinks-
974 Robertson. A. Gusa was funded by the NIH Tri-Institutional Molecular Mycology and
975 Pathogenesis Training Program grant T32AI052080 and the NIH/NIAID grant K99/R00AI166094
976 grant awarded to A. Gusa. Additional support to A. Gusa was provided by the Canadian Institute
977 for Advanced Research (CIFAR) Azrieli Global Scholars program and the Duke University
978 Whitehead Scholars award. C. Feschotte and J.F. McCormick were supported by NIH grant
979 R35GM122550. J. Perfect was supported by NIH/NIAID AI-73896 and AI-93257. P. Magwene
980 was supported by NIH/NIAID grant R01AI133654.

981 The isolates from patients with recurrent cryptococcal meningitis in this study were
982 collected through GERMS-SA surveillance, provided by Dr. N.P. Govender of the National
983 Institute for Communicable Diseases, South Africa, and shared by Dr. J. Perfect at Duke
984 University. Members of GERMS-SA, 2005 to 2008, included S. Vasaikar (Eastern Cape); N.
985 Janse van Rensberg, A. Möller, P. Smith, and A. M. Pretorius (Free State); K. Ahmed, A.
986 Hoosen, R. Lekalakala, P. P. Sein, C. Feldman, A. S. Karstaedt, O. Perovic, J. Wadula, M. Dove,
987 K. Lindeque, L. Meyer, and G. Weldhagen (Gauteng); S. Harvey and P. Jooste (Northern Cape);
988 D. Cilliers and A. Rampe (North West Province); W. Sturm, T. Vanmali, P. Bhola, P. Moodley, S.
989 Sithole, and H. Dawood (KwaZulu Natal); K. Hamese (Limpopo); K. Bauer, G. Hoyland, J.
990 Lebudi, and C. Mutanda (Mpumalanga); R. Hoffmann, S. Martin, L. Liebowitz, and E.
991 Wasserman (Western Cape); A. Whitelaw (Western Cape); A. Brink, I. Zietsman, M. Botha, X.
992 Poswa, M. da Silva, and S. Budavari (Ampath laboratories); C. Heney and J. Smit (Lancet

laboratories); M. Senekal (Pathcare laboratories); A. Schuchat and S. Schrag (CDC); K. P. Klugman (Emory); and C. Cohen, L. Dini, L. de Gouveia, J. Frean, S. Gould, K. Keddy, K. M. McCarthy, J. Patel, S. T. Meiring, E. G. Prentice, V. C. Quan, J. Ramalivhana, A. Sooka, A. von Gottberg, and N. P. Govender (National Institute for Communicable Diseases). In South Africa, the work was partially funded from 2005 through 2006 by the U.S. Agency for International Development's Antimicrobial Resistance Initiative, transferred via Cooperative Agreement U60/CCU022088 from the U.S. Centers for Disease Control and Prevention (CDC), Atlanta, GA. From 2005 through 2008, the study was also partially supported by the CDC, National Center for HIV/AIDS, Viral Hepatitis, STD, and TB Prevention (NCHHSTP) and the Global AIDS Program (GAP) Cooperative Agreement U62/PSO022901.

COMPETING INTERESTS

The authors declare no competing interests.

REFERENCES

1. Feng G, Leem Y-E, Levin HL. Transposon integration enhances expression of stress response genes. Nucleic Acids Res. 2013 Jan;41(2):775–789.

2. Esnault C, Lee M, Ham C, Levin HL. Transposable element insertions in fission yeast drive adaptation to environmental stress. Genome Res. 2019 Jan;29(1):85–95.

3. Urquhart AS, Chong NF, Yang Y, Idnurm A. A large transposable element mediates metal resistance in the fungus Paecilomyces variotii. Curr Biol. 2022 Jan 17;

4. McDonald MC, Taranto AP, Hill E, Schwessinger B, Liu Z, Simpfendorfer S, et al. Transposon-Mediated Horizontal Transfer of the Host-Specific Virulence Protein ToxA between Three Fungal Wheat Pathogens. MBio. 2019 Sep 10;10(5).

5. Hays M, Schwartz K, Schmidtke DT, Aggeli D, Sherlock G. Paths to adaptation under fluctuating nitrogen starvation: The spectrum of adaptive mutations in Saccharomyces cerevisiae is shaped by retrotransposons and microhomology-mediated recombination. PLoS Genet. 2023 May 16;19(5):e1010747.

6. Singh NK, Badet T, Abraham L, Croll D. Rapid sequence evolution driven by transposable elements at a virulence locus in a fungal wheat pathogen. BMC Genomics. 2021 May 27;22(1):393.

7. Oggenfuss U, Croll D. Recent transposable element bursts are associated with the proximity to genes in a fungal plant pathogen. PLoS Pathog. 2023 Feb 14;19(2):e1011130.

1027 8. Lorrain C, Feurtey A, Möller M, Haueisen J, Stukenbrock E. Dynamics of transposable
1028 elements in recently diverged fungal pathogens: lineage-specific transposable element
1029 content and efficiency of genome defenses. G3 (Bethesda). 2021 Apr 15;11(4).

1030 9. Wells JN, Feschotte C. A field guide to eukaryotic transposable elements. Annu Rev
1031 Genet. 2020 Nov 23;54:539–561.

1032 10. Bourque G, Burns KH, Gehring M, Gorbunova V, Seluanov A, Hammell M, et al. Ten
1033 things you should know about transposable elements. Genome Biol. 2018 Nov
1034 19;19(1):199.

1035 11. Gluck-Thaler E, Ralston T, Konkel Z, Ocampos CG, Ganeshan VD, Dorrance AE, et al.
1036 Giant starship elements mobilize accessory genes in fungal genomes. Mol Biol Evol.
1037 2022 May 3;39(5).

1038 12. Baduel P, Sammarco I, Barrett R, Coronado-Zamora M, Crespel A, Díez-Rodríguez B, et
1039 al. The evolutionary consequences of interactions between the epigenome, the genome
1040 and the environment. Evol Appl. 2024 Jul 23;17(7):e13730.

1041 13. Horváth V, Merenciano M, González J. Revisiting the Relationship between
1042 Transposable Elements and the Eukaryotic Stress Response. Trends Genet. 2017
1043 Nov;33(11):832–841.

1044 14. Fouché S, Badet T, Oggenfuss U, Plissonneau C, Francisco CS, Croll D. Stress-Driven
1045 Transposable Element De-repression Dynamics and Virulence Evolution in a Fungal
1046 Pathogen. Mol Biol Evol. 2020 Jan 1;37(1):221–239.

1047 15. Sehgal A, Lee C-YS, Espenshade PJ. SREBP controls oxygen-dependent mobilization of
1048 retrotransposons in fission yeast. PLoS Genet. 2007 Aug;3(8):e131.

1049 16. Paquin CE, Williamson VM. Temperature effects on the rate of ty transposition. Science.
1050 1984 Oct 5;226(4670):53–55.

1051 17. Servant G, Pinson B, Tchalikian-Cosson A, Coulpier F, Lemoine S, Pennetier C, et al.
1052 Tye7 regulates yeast Ty1 retrotransposon sense and antisense transcription in response
1053 to adenylic nucleotides stress. Nucleic Acids Res. 2012 Jul;40(12):5271–5282.

1054 18. Lin X, Heitman J. The biology of the Cryptococcus neoformans species complex. Annu
1055 Rev Microbiol. 2006;60:69–105.

1056 19. Goodwin TJ, Poulter RT. The diversity of retrotransposons in the yeast Cryptococcus
1057 neoformans. Yeast. 2001 Jun 30;18(9):865–880.

1058 20. Goodwin TJD, Butler MI, Poulter RTM. Cryptons: a group of tyrosine-recombinase-
1059 encoding DNA transposons from pathogenic fungi. Microbiology (Reading, Engl). 2003
1060 Nov;149(Pt 11):3099–3109.

1061 21. Rajasingham R, Smith RM, Park BJ, Jarvis JN, Govender NP, Chiller TM, et al. Global
1062 burden of disease of HIV-associated cryptococcal meningitis: an updated analysis.
1063 Lancet Infect Dis. 2017 Aug;17(8):873–881.

1064 22. Denning DW. Global incidence and mortality of severe fungal disease. Lancet Infect Dis.
1065 2024 Jul;24(7):e428–e438.

1066 23. Chang CC, Dorasamy AA, Gosnell BI, Elliott JH, Spelman T, Omarjee S, et al. Clinical
1067 and mycological predictors of cryptococcosis-associated immune reconstitution
1068 inflammatory syndrome. AIDS. 2013 Aug 24;27(13):2089–2099.

1069 24. Chen Y, Farrer RA, Giamberardino C, Sakthikumar S, Jones A, Yang T, et al.
1070 Microevolution of Serial Clinical Isolates of Cryptococcus neoformans var. grubii and
1071 C. gattii. MBio. 2017 Mar 7;8(2).

1072 25. Ormerod KL, Morrow CA, Chow EWL, Lee IR, Arras SDM, Schirra HJ, et al. Comparative
1073 Genomics of Serial Isolates of Cryptococcus neoformans Reveals Gene Associated With
1074 Carbon Utilization and Virulence. G3 (Bethesda). 2013 Apr 9;3(4):675–686.

1075 26. Sephton-Clark P, McConnell SA, Grossman N, Baker RP, Dragotakes Q, Fan Y, et al.
1076 Similar evolutionary trajectories in an environmental Cryptococcus neoformans isolate
1077 after human and murine infection. Proc Natl Acad Sci USA. 2023 Jan
1078 10;120(2):e2217111120.

1079 27. Hu G, Chen SH, Qiu J, Bennett JE, Myers TG, Williamson PR. Microevolution during
1080 serial mouse passage demonstrates FRE3 as a virulence adaptation gene in
1081 Cryptococcus neoformans. MBio. 2014 Apr 1;5(2):e00941–14.

1082 28. Ewing AD. Transposable element detection from whole genome sequence data. Mob
1083 DNA. 2015 Dec 29;6:24.

1084 29. Brown SM, Campbell LT, Lodge JK. Cryptococcus neoformans, a fungus under stress.
1085 Curr Opin Microbiol. 2007 Aug 17;10(4):320–325.

1086 30. Gusa A, Williams JD, Cho J-E, Averette AF, Sun S, Shouse EM, et al. Transposon
1087 mobilization in the human fungal pathogen Cryptococcus is mutagenic during infection
1088 and promotes drug resistance in vitro. Proc Natl Acad Sci USA. 2020 May
1089 5;117(18):9973–9980.

1090 31. Gusa A, Yadav V, Roth C, Williams JD, Shouse EM, Magwene P, et al. Genome-wide
1091 analysis of heat stress-stimulated transposon mobility in the human fungal pathogen
1092 Cryptococcus deneoformans. Proc Natl Acad Sci USA. 2023 Jan
1093 24;120(4):e2209831120.

1094 32. Huang J, Larmore CJ, Priest SJ, Xu Z, Dietrich FS, Yadav V, et al. Distinct evolutionary
1095 trajectories following loss of RNA interference in Cryptococcus neoformans. Proc Natl
1096 Acad Sci USA. 2024 Nov 19;121(47):e2416656121.

1097 33. Maziarz EK, Perfect JR. Cryptococcosis. Infect Dis Clin North Am. 2016 Mar;30(1):179–
1098 206.

1099 34. Wang X, Hsueh Y-P, Li W, Floyd A, Skalsky R, Heitman J. Sex-induced silencing defends
1100 the genome of Cryptococcus neoformans via RNAi. Genes Dev. 2010 Nov
1101 15;24(22):2566–2582.

1102 35. Dumesic PA, Natarajan P, Chen C, Drinnenberg IA, Schiller BJ, Thompson J, et al.
1103 Stalled spliceosomes are a signal for RNAi-mediated genome defense. Cell. 2013 Feb
1104 28;152(5):957–968.

1105 36. Burke JE, Longhurst AD, Natarajan P, Rao B, Liu J, Sales-Lee J, et al. A Non-Dicer
1106 RNase III and Four Other Novel Factors Required for RNAi-Mediated Transposon
1107 Suppression in the Human Pathogenic Yeast Cryptococcus neoformans. G3 (Bethesda).
1108 2019 Jul 9;9(7):2235–2244.

1109 37. Janbon G, Maeng S, Yang D-H, Ko Y-J, Jung K-W, Moyrand F, et al. Characterizing the
1110 role of RNA silencing components in Cryptococcus neoformans. Fungal Genet Biol. 2010
1111 Dec;47(12):1070–1080.

1112 38. Priest SJ, Yadav V, Roth C, Dahlmann TA, Kück U, Magwene PM, et al. Uncontrolled
1113 transposition following RNAi loss causes hypermutation and antifungal drug resistance in
1114 clinical isolates of Cryptococcus neoformans. Nat Microbiol. 2022 Aug 2;7(8):1239–1251.

1115 39. Yadav V, Sun S, Billmyre RB, Thimmappa BC, Shea T, Lintner R, et al. RNAi is a critical
1116 determinant of centromere evolution in closely related fungi. Proc Natl Acad Sci USA.
1117 2018 Mar 20;115(12):3108–3113.

1118 40. Schotanus K, Yadav V, Heitman J. Epigenetic dynamics of centromeres and
1119 neocentromeres in Cryptococcus deuterogattii. PLoS Genet. 2021 Aug
1120 31;17(8):e1009743.

1121 41. Catania S, Dumesic PA, Pimentel H, Nasif A, Stoddard CI, Burke JE, et al. Evolutionary
1122 Persistence of DNA Methylation for Millions of Years after Ancient Loss of a De Novo
1123 Methyltransferase. Cell. 2020 Jan 23;180(2):263–277.e20.

1124 42. Dumesic PA, Homer CM, Moresco JJ, Pack LR, Shanle EK, Coyle SM, et al. Product
1125 binding enforces the genomic specificity of a yeast polycomb repressive complex. Cell.
1126 2015 Jan 15;160(1-2):204–218.

1127 43. Desjardins CA, Giamberardino C, Sykes SM, Yu C-H, Tenor JL, Chen Y, et al. Population
1128 genomics and the evolution of virulence in the fungal pathogen Cryptococcus
1129 neoformans. Genome Res. 2017 Jul;27(7):1207–1219.

1130 44. Van Wyk M, Govender NP, Mitchell TG, Litvintseva AP, GERMS-SA. Multilocus sequence
1131 typing of serially collected isolates of Cryptococcus from HIV-infected patients in South
1132 Africa. J Clin Microbiol. 2014 Jun;52(6):1921–1931.

1133 45. Bovers M, Hagen F, Kuramae EE, Boekhout T. Six monophyletic lineages identified
1134 within Cryptococcus neoformans and Cryptococcus gattii by multi-locus sequence typing.
1135 Fungal Genet Biol. 2008 Apr;45(4):400–421.

1136 46. WHO fungal priority' ' pathogens list to guide research, development and public health
1137 actio.

1138 47. Cruz MC, Cavallo LM, Görlach JM, Cox G, Perfect JR, Cardenas ME, et al. Rapamycin
1139 antifungal action is mediated via conserved complexes with FKBP12 and TOR kinase
1140 homologs in Cryptococcus neoformans. Mol Cell Biol. 1999 Jun;19(6):4101–4112.

1141 48. Wicker T, Sabot F, Hua-Van A, Bennetzen JL, Capy P, Chalhoub B, et al. A unified
1142 classification system for eukaryotic transposable elements. Nat Rev Genet. 2007
1143 Dec;8(12):973–982.

1144 49. Kent WJ. BLAT--the BLAST-like alignment tool. Genome Res. 2002 Apr;12(4):656–664.

1145 50. Goel M, Sun H, Jiao W-B, Schneeberger K. SyRI: finding genomic rearrangements and
1146 local sequence differences from whole-genome assemblies. Genome Biol. 2019 Dec
1147 16;20(1):277.

1148 51. Fedoroff NV. Molecular genetics and epigenetics of CACTA elements. Methods Mol Biol.
1149 2013;1057:177–192.

1150 52. Yuan Y-W, Wessler SR. The catalytic domain of all eukaryotic cut-and-paste transposase
1151 superfamilies. Proc Natl Acad Sci USA. 2011 May 10;108(19):7884–7889.

1152 53. Iyer LM, Zhang D, de Souza RF, Pukkila PJ, Rao A, Aravind L. Lineage-specific
1153 expansions of TET/JBP genes and a new class of DNA transposons shape fungal
1154 genomic and epigenetic landscapes. Proc Natl Acad Sci USA. 2014 Feb 4;111(5):1676–
1155 1683.

1156 54. Coffin JM, Hughes SH, Varmus HE. Structural Classes of Retroelements and Replication
1157 Strategies. 1997;

1158 55. Eickbush TH, Jamburuthugoda VK. The diversity of retrotransposons and the properties
1159 of their reverse transcriptases. Virus Res. 2008 Jun;134(1-2):221–234.

1160 56. Cost GJ, Feng Q, Jacquier A, Boeke JD. Human L1 element target-primed reverse
1161 transcription in vitro. EMBO J. 2002 Nov 1;21(21):5899–5910.

1162 57. Priest SJ, Coelho MA, Mixão V, Clancey SA, Xu Y, Sun S, et al. Factors enforcing the
1163 species boundary between the human pathogens Cryptococcus neoformans and
1164 Cryptococcus deneoformans. PLoS Genet. 2021 Jan 19;17(1):e1008871.

1165 58. Yang J, Malik HS, Eickbush TH. Identification of the endonuclease domain encoded by
1166 R2 and other site-specific, non-long terminal repeat retrotransposable elements. Proc
1167 Natl Acad Sci USA. 1999 Jul 6;96(14):7847–7852.

1168 59. Christensen SM, Ye J, Eickbush TH. RNA from the 5’ end of the R2 retrotransposon
1169 controls R2 protein binding to and cleavage of its DNA target site. Proc Natl Acad Sci
1170 USA. 2006 Nov 21;103(47):17602–17607.

1171 60. Fujiwara H. Site-specific non-LTR retrotransposons. Microbiol Spectr. 2015
1172 Apr;3(2):MDNA3–0001.

1173 61. Jurka J. Sequence patterns indicate an enzymatic involvement in integration of
1174 mammalian retroposons. Proc Natl Acad Sci USA. 1997 Mar 4;94(5):1872–1877.

1175 62. Starnes JH, Thornbury DW, Novikova OS, Rehmeyer CJ, Farman ML. Telomere-targeted
1176 retrotransposons in the rice blast fungus Magnaporthe oryzae: agents of telomere
1177 instability. Genetics. 2012 Jun;191(2):389–406.

1178 63. Korotko U, Chwiałkowska K, Sańko-Sawczenko I, Kwasniewski M. DNA Demethylation in
1179 Response to Heat Stress in Arabidopsis thaliana. Int J Mol Sci. 2021 Feb 4;22(4).

1180 64. Zhang L, Yan L, Jiang J, Wang Y, Jiang Y, Yan T, et al. The structure and
1181 retrotransposition mechanism of LTR-retrotransposons in the asexual yeast Candida
1182 albicans. Virulence. 2014 Aug 15;5(6):655–664.

1183 65. Yang D-H, Jung K-W, Bang S, Lee J-W, Song M-H, Floyd-Averette A, et al. Rewiring of
1184 Signaling Networks Modulating Thermotolerance in the Human Pathogen Cryptococcus
1185 neoformans. Genetics. 2017 Jan;205(1):201–219.

1186 66. Kang YS, Jung J, Brown HL, Mateusiak C, Doering TL, Brent MR. Leveraging a new data
1187 resource to define the response of Cryptococcus neoformans to environmental signals.
1188 Genetics. 2025 Jan 8;229(1):1–29.

1189 67. Nosanchuk JD, Shoham S, Fries BC, Shapiro DS, Levitz SM, Casadevall A. Evidence of
1190 zoonotic transmission of Cryptococcus neoformans from a pet cockatoo to an
1191 immunocompromised patient. Ann Intern Med. 2000 Feb 1;132(3):205–208.

1192 68. Baril T, Galbraith J, Hayward A. Earl Grey: A Fully Automated User-Friendly Transposable
1193 Element Annotation and Analysis Pipeline. Mol Biol Evol. 2024 Apr 2;41(4).

1194 69. Kim JM, Vanguri S, Boeke JD, Gabriel A, Voytas DF. Transposable elements and
1195 genome organization: a comprehensive survey of retrotransposons revealed by the
1196 complete Saccharomyces cerevisiae genome sequence. Genome Res. 1998
1197 May;8(5):464–478.

1198 70. Levin HL, Weaver DC, Boeke JD. Two related families of retrotransposons from
1199 Schizosaccharomyces pombe. Mol Cell Biol. 1990 Dec;10(12):6791–6798.

1200 71. Curcio MJ, Lutz S, Lesage P. The Ty1 LTR-retrotransposon of budding yeast,
1201 Saccharomyces cerevisiae. Microbiol Spectr. 2015 Apr 1;3(2):1–35.

1202 72. Curcio MJ, Garfinkel DJ. Single-step selection for Ty1 element retrotransposition. Proc
1203 Natl Acad Sci USA. 1991 Feb 1;88(3):936–940.

1204 73. Behrens R, Hayles J, Nurse P. Fission yeast retrotransposon Tf1 integration is targeted
1205 to 5’ ends of open reading frames. Nucleic Acids Res. 2000 Dec 1;28(23):4709–4716.

1206 74. Singleton TL, Levin HL. A long terminal repeat retrotransposon of fission yeast has strong
1207 preferences for specific sites of insertion. Eukaryotic Cell. 2002 Feb;1(1):44–55.

1208 75. McClintock B. The origin and behavior of mutable loci in maize. Proc Natl Acad Sci USA.
1209 1950 Jun;36(6):344–355.

1210 76. Cordaux R, Batzer MA. The impact of retrotransposons on human genome evolution. Nat
1211 Rev Genet. 2009 Oct;10(10):691–703.

1212 77. Thomas J, Vadnagara K, Pritham EJ. DINE-1, the highest copy number repeats in
1213 Drosophila melanogaster are non-autonomous endonuclease-encoding rolling-circle
1214 transposable elements (Helentrons). Mob DNA. 2014 Jun 4;5:18.

1215 78. Feschotte C, Jiang N, Wessler SR. Plant transposable elements: where genetics meets
1216 genomics. Nat Rev Genet. 2002 May;3(5):329–341.

1217 79. Tsukahara S, Bousios A, Perez-Roman E, Yamaguchi S, Leduque B, Nakano A, et al.
1218 Centrophilic retrotransposon integration via CENH3 chromatin in Arabidopsis. Nature.
1219 2025 Jan 1;637(8046):744–748.

1220 80. Dai J, Xie W, Brady TL, Gao J, Voytas DF. Phosphorylation regulates integration of the
1221 yeast Ty5 retrotransposon into heterochromatin. Mol Cell. 2007 Jul 20;27(2):289–299.

1222 81. Cavrak VV, Lettner N, Jamge S, Kosarewicz A, Bayer LM, Mittelsten Scheid O. How a
1223 retrotransposon exploits the plant's heat stress response for its activation. PLoS Genet.
1224 2014 Jan 30;10(1):e1004115.

1225 82. Pietzenuk B, Markus C, Gaubert H, Bagwan N, Merotto A, Bucher E, et al. Recurrent
1226 evolution of heat-responsiveness in Brassicaceae COPIA elements. Genome Biol. 2016
1227 Oct 11;17(1):209.

1228 83. Garrigues JM, Tsu BV, Daugherty MD, Pasquinelli AE. Diversification of the
1229 Caenorhabditis heat shock response by Helitron transposable elements. Elife. 2019 Dec
1230 11;8.

1231 84. Lawler JF, Haeusser DP, Dull A, Boeke JD, Keeney JB. Ty1 defect in proteolysis at high
1232 temperature. J Virol. 2002 May;76(9):4233–4240.

1233 85. Cappucci U, Noro F, Casale AM, Fanti L, Berloco M, Alagia AA, et al. The Hsp70
1234 chaperone is a major player in stress-induced transposable element activation. Proc Natl
1235 Acad Sci USA. 2019 Sep 3;116(36):17943–17950.

1236 86. Yadav V, Mohan R, Sun S, Heitman J. Calcineurin contributes to RNAi-mediated
1237 transgene silencing and small interfering RNA production in the human fungal pathogen
1238 Cryptococcus neoformans. Genetics. 2024 Jan 27;

1239 87. Hall BM, Ma C-X, Liang P, Singh KK. Fluctuation analysis CalculatOR: a web tool for the
1240 determination of mutation rate using Luria-Delbruck fluctuation analysis. Bioinformatics.
1241 2009 Jun 15;25(12):1564–1565.

1242 88. Hommelsheim CM, Frantzeskakis L, Huang M, Ülker B. PCR amplification of repetitive
1243 DNA: a limitation to genome editing technologies and many other applications. Sci Rep.
1244 2014 May 23;4:5052.

1245 89. Hum YF, Jinks-Robertson S. DNA strand-exchange patterns associated with double-
1246 strand break-induced and spontaneous mitotic crossovers in Saccharomyces cerevisiae.
1247 PLoS Genet. 2018 Mar 26;14(3):e1007302.

1248 90. Moore A, Dominska M, Greenwell P, Aksenova AY, Mirkin S, Petes T. Genetic control of
1249 genomic alterations induced in yeast by interstitial telomeric sequences. Genetics. 2018
1250 Apr 2;209(2):425–438.

1251 91. Tamura K, Stecher G, Kumar S. MEGA11: Molecular Evolutionary Genetics Analysis
1252 version 11. Mol Biol Evol. 2021 Jun 25;38(7):3022–3027.

1253 92. Pitkin JW, Panaccione DG, Walton JD. A putative cyclic peptide efflux pump encoded by
1254 the TOXA gene of the plant-pathogenic fungus Cochliobolus carbonum. Microbiology
1255 (Reading, Engl). 1996 Jun;142 (Pt 6):1557–1565.

1256 93. Koren S, Walenz BP, Berlin K, Miller JR, Bergman NH, Phillippy AM. Canu: scalable and
1257 accurate long-read assembly via adaptive k-mer weighting and repeat separation.
1258 Genome Res. 2017 May;27(5):722–736.

1259 94. Kolmogorov M, Yuan J, Lin Y, Pevzner PA. Assembly of long, error-prone reads using
1260 repeat graphs. Nat Biotechnol. 2019 May;37(5):540–546.

1261 95. Li H. Minimap2: pairwise alignment for nucleotide sequences. Bioinformatics. 2018 Sep
1262 15;34(18):3094–3100.

1263 96. Langmead B, Salzberg SL. Fast gapped-read alignment with Bowtie 2. Nat Methods.
1264 2012 Mar 4;9(4):357–359.

1265 97. Walker BJ, Abeel T, Shea T, Priest M, Abouelliel A, Sakthikumar S, et al. Pilon: an
1266 integrated tool for comprehensive microbial variant detection and genome assembly
1267 improvement. PLoS One. 2014 Nov 19;9(11):e112963.

1268 98. Robinson JT, Thorvaldsdóttir H, Winckler W, Guttman M, Lander ES, Getz G, et al.
1269 Integrative genomics viewer. Nat Biotechnol. 2011 Jan;29(1):24–26.

1270 99. Janbon G, Ormerod KL, Paulet D, Byrnes EJ, Yadav V, Chatterjee G, et al. Analysis of
1271 the genome and transcriptome of Cryptococcus neoformans var. grubii reveals complex
1272 RNA expression and microevolution leading to virulence attenuation. PLoS Genet. 2014
1273 Apr 17;10(4):e1004261.

1274 100. Altschul SF, Gish W, Miller W, Myers EW, Lipman DJ. Basic local alignment search tool.
1275 J Mol Biol. 1990 Oct 5;215(3):403–410.

1276 101. Camacho C, Coulouris G, Avagyan V, Ma N, Papadopoulos J, Bealer K, et al. BLAST+:
1277 architecture and applications. BMC Bioinformatics. 2009 Dec 15;10:421.

1278 102. Goel M, Schneeberger K. plotsr: visualizing structural similarities and rearrangements
1279 between multiple genomes. Bioinformatics. 2022 May 13;38(10):2922–2926.

1280 103. Kohany O, Gentles AJ, Hankus L, Jurka J. Annotation, submission and screening of
1281 repetitive elements in Repbase: RepbaseSubmitter and Censor. BMC Bioinformatics.
1282 2006 Oct 25;7:474.

1283 104. Shumate A, Salzberg SL. Liftoff: accurate mapping of gene annotations. Bioinformatics.
1284 2021 Jul 19;37(12):1639–1643.

1285 105. Pedersen BS, Quinlan AR. Mosdepth: quick coverage calculation for genomes and
1286 exomes. Bioinformatics. 2018 Mar 1;34(5):867–868.

1287

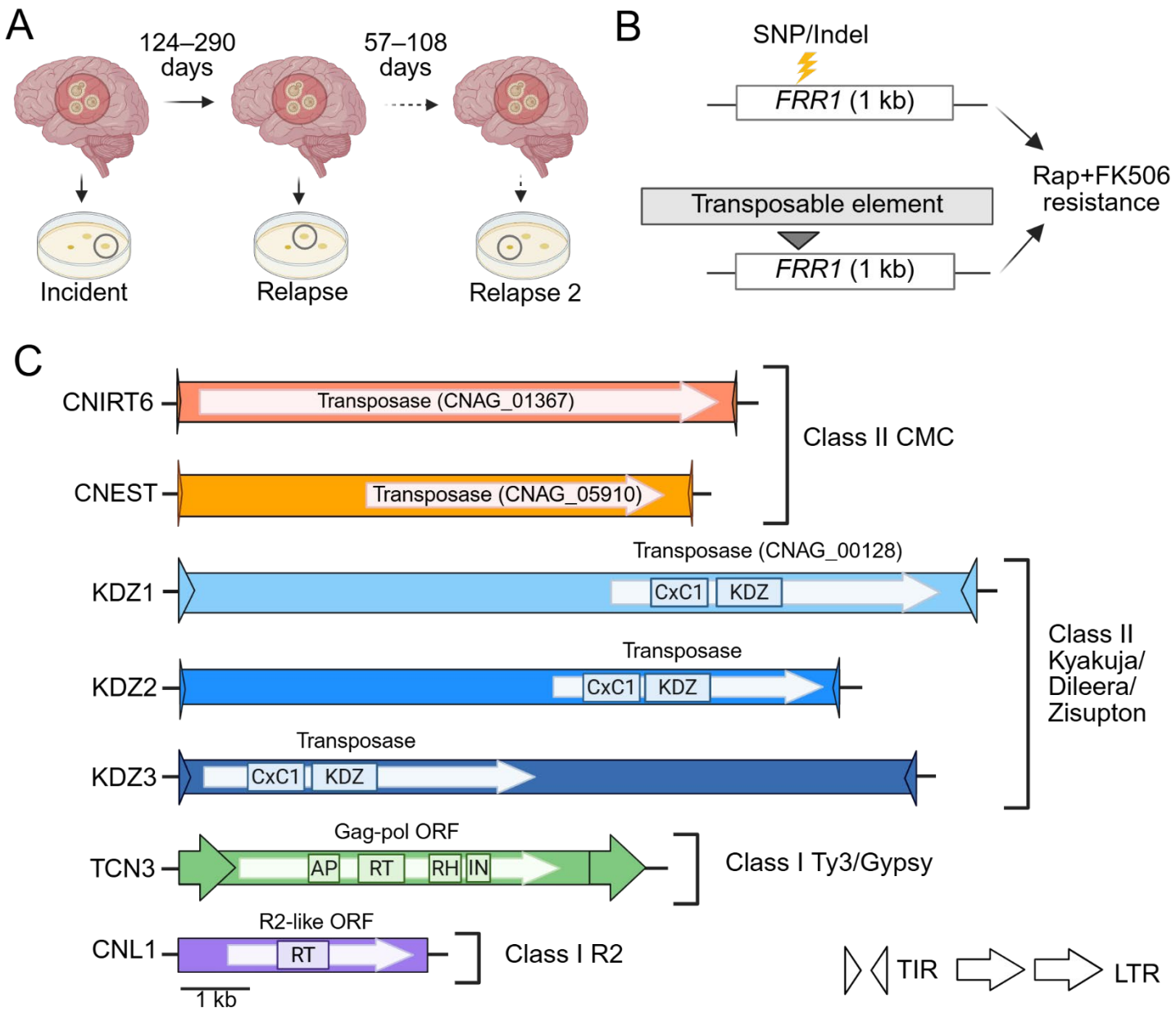

Figure 1. Diverse transposable elements (TEs) captured mobilizing in clinical isolates of *C. neoformans*. (**A**) Schematic of clinical isolate collection from patients with recurrent cryptococcal meningitis at disease onset and after subsequent relapse(s). Single colonies were isolated from patient cerebrospinal fluid. (**B**) Diagram of the "transposon trap" assay. Point mutations or TE insertions in the *FRR1* reporter gene confer resistance to rapamycin and FK506 (rap+FK506). (**C**) Illustration of seven mobile TEs, including class II elements from the CMC (CACTA, Mirage, Chapaev) supergroup and Kyakuja/Dileera/Zisupton superfamily, and class I elements from the Ty3/gypsy and R2 superfamilies. Terminal inverted repeats (TIRs) and long terminal repeats (LTRs) are indicated by triangles and arrows, respectively. Genes within TEs that are predicted to facilitate mobilization are shown as white arrows. Functional domains are indicated, including KDZ (Kyakuja/Dileera/Zisupton transposase), CxC1 (predicted zinc chelating domain), AP (aspartic protease), RT (reverse transcriptase), RH (RNase H), and IN (integrase). TEs are drawn to scale.

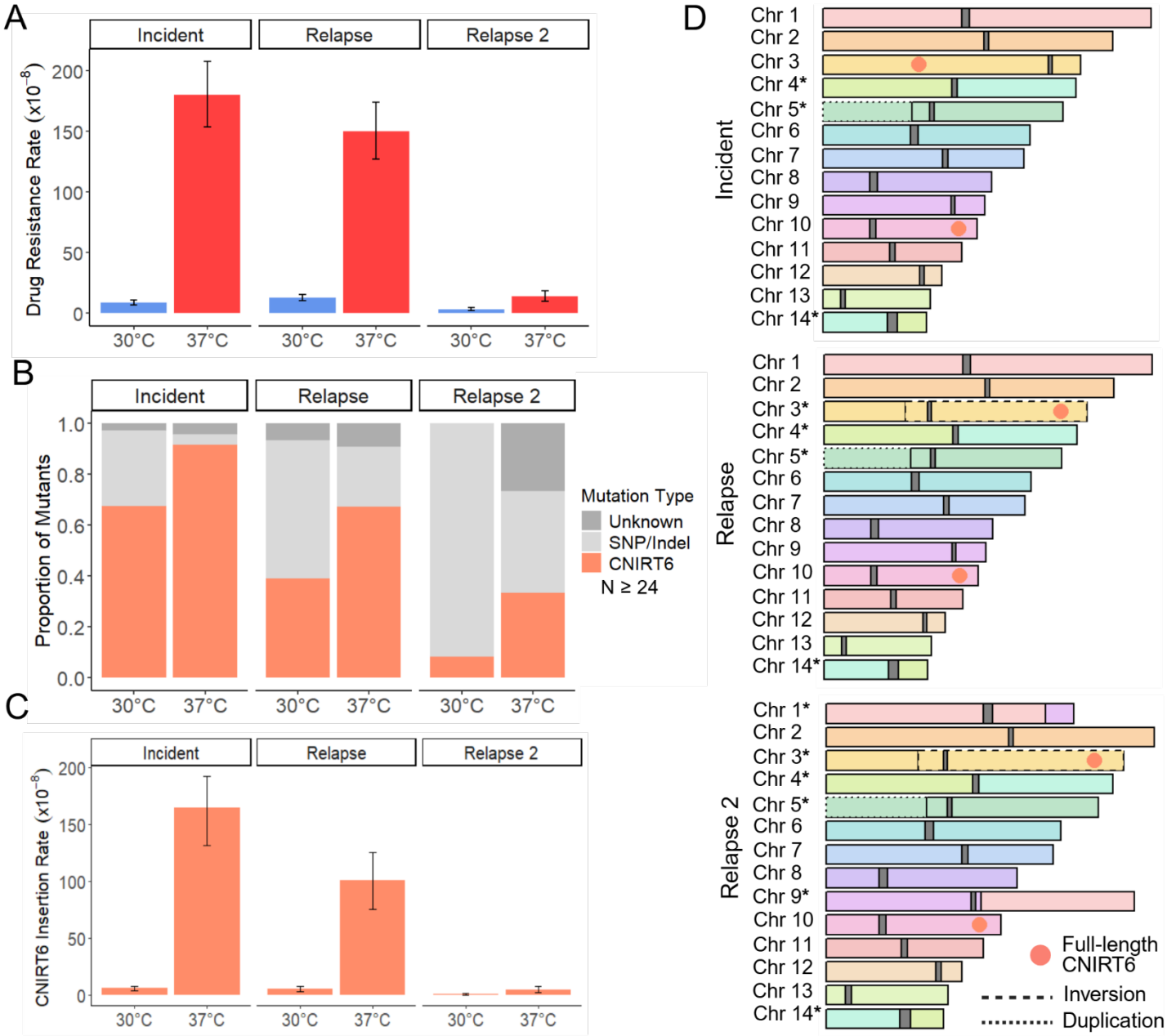

Figure 2. Mobilization of the DNA transposon CNIRT6 is induced by heat stress. (**A**) Rap+FK506 drug resistance rates following growth in non-selective YPD medium at 30°C or 37°C. (**B**) Mutation spectra in the *FRR1* gene for independent rap+FK506-resistant mutants. The mutation type "Unknown" indicates failure to amplify *FRR1* or absence of detectable mutations in its sequence (N = 24 – 55). (**C**) Insertion rate of CNIRT6 into *FRR1*. (**D**) Karyograms of the case 15 incident, relapse, and relapse 2 isolates. Full-length copies of CNIRT6 are shown as orange circles. Chromosome synteny is indicated by chromosome color, with inversions and duplications outlined in dashed and dotted lines, respectively. All chromosomes with identified structural rearrangements are marked with an asterisk. Error bars represent 95% confidence intervals (CIs); rates are considered statistically different if error bars do not overlap.

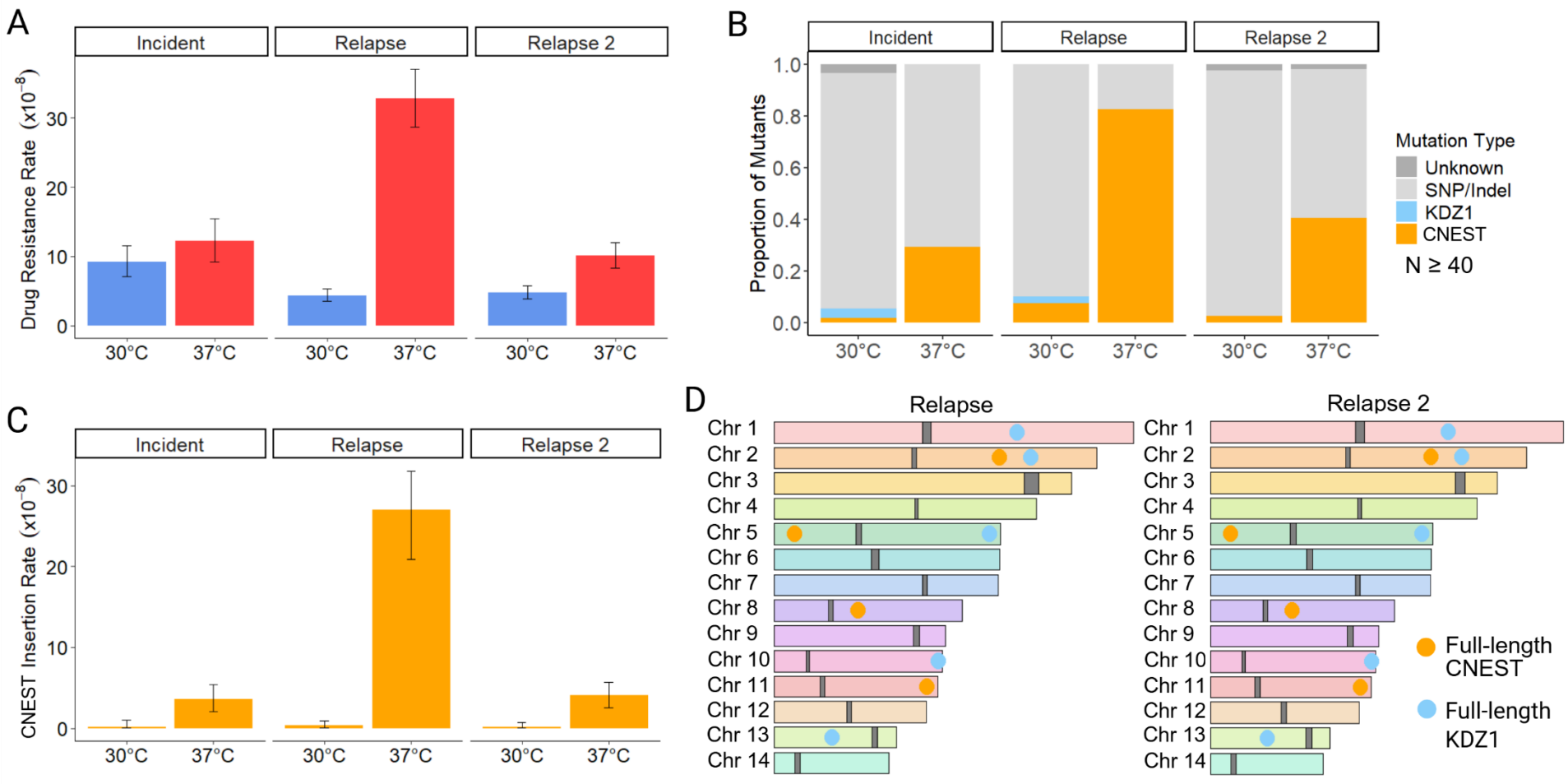

Figure 3. Mobilization of the DNA transposon CNEST is induced by heat stress. (**A**) Rap+FK506 drug resistance rates following growth in non-selective YPD medium at 30°C or 37°C. (**B**) Mutation spectra in the *FRR1* gene for independent rap+FK506-resistant mutants. The mutation type "Unknown" indicates failure to amplify *FRR1* or absence of detectable mutations in its sequence (N = 40 – 65). (**C**) Insertion rate of CNEST into *FRR1*. (**D**) Karyograms of the case 77 relapse and relapse 2 isolates. Full-length copies of CNEST (yellow) and KDZ1 (light blue) are shown as circles. Chromosome synteny is indicated by chromosome color. Error bars represent 95% confidence intervals (CIs); rates are considered statistically different if error bars do not overlap.

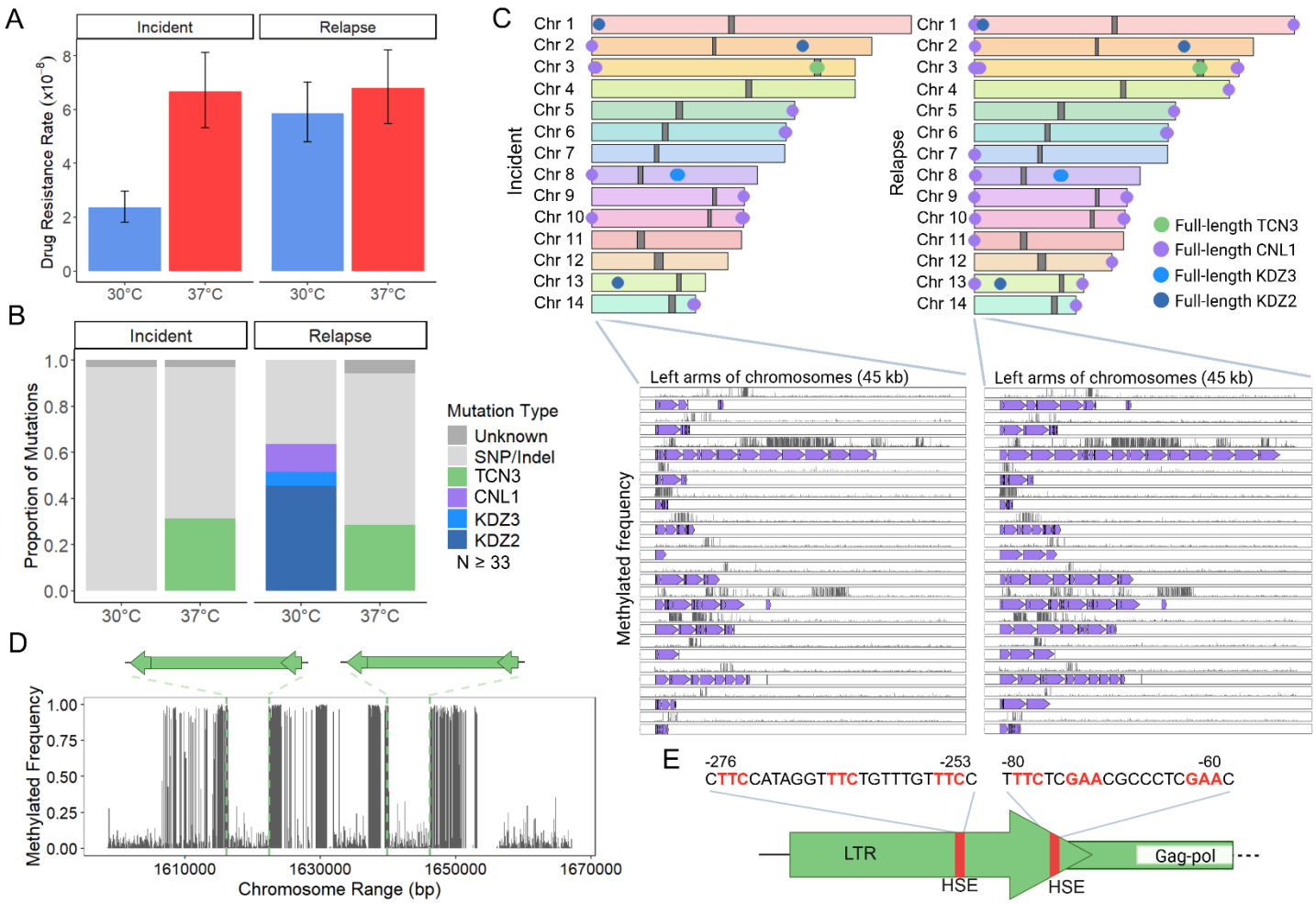

Figure 4. Temperature- and strain-specific TE dynamics in case 7. (**A**) Rap+FK506 drug resistance rates following growth in non-selective YPD medium at 30°C or 37°C. (**B**) Mutation spectra in the *FRR1* gene for independent rap+FK506-resistant mutants. The mutation type "Unknown" indicates failure to amplify *FRR1* or absence of detectable mutations in its sequence (N = 33 – 35). (**C**) Karyograms of the case 7 incident and relapse isolates. Full-length copies of TCN3 (green), CNL1 (purple), KDZ3 (blue), and KDZ2 (dark blue) are shown as circles. Chromosome synteny is indicated by chromosome color. Insets show the 45 kb regions on the left arms of chromosomes in the incident and relapse isolates. Purple arrows indicate all CNL1 BLASTn hits; grey lines represent DNA methylation frequency from long reads, with the y-axis scaled from 0 to 1. (**D**) DNA methylation frequency plotted for the Chr 3 centromere region ±10 kb of the incident isolate. The position and orientation of full-length TCN3 copies is shown. (**E**) Diagram of HSE sequence motifs (red) identified in TCN3 LTRs. Position is shown relative to the gag-pol open reading frame (ORF) translation start site.

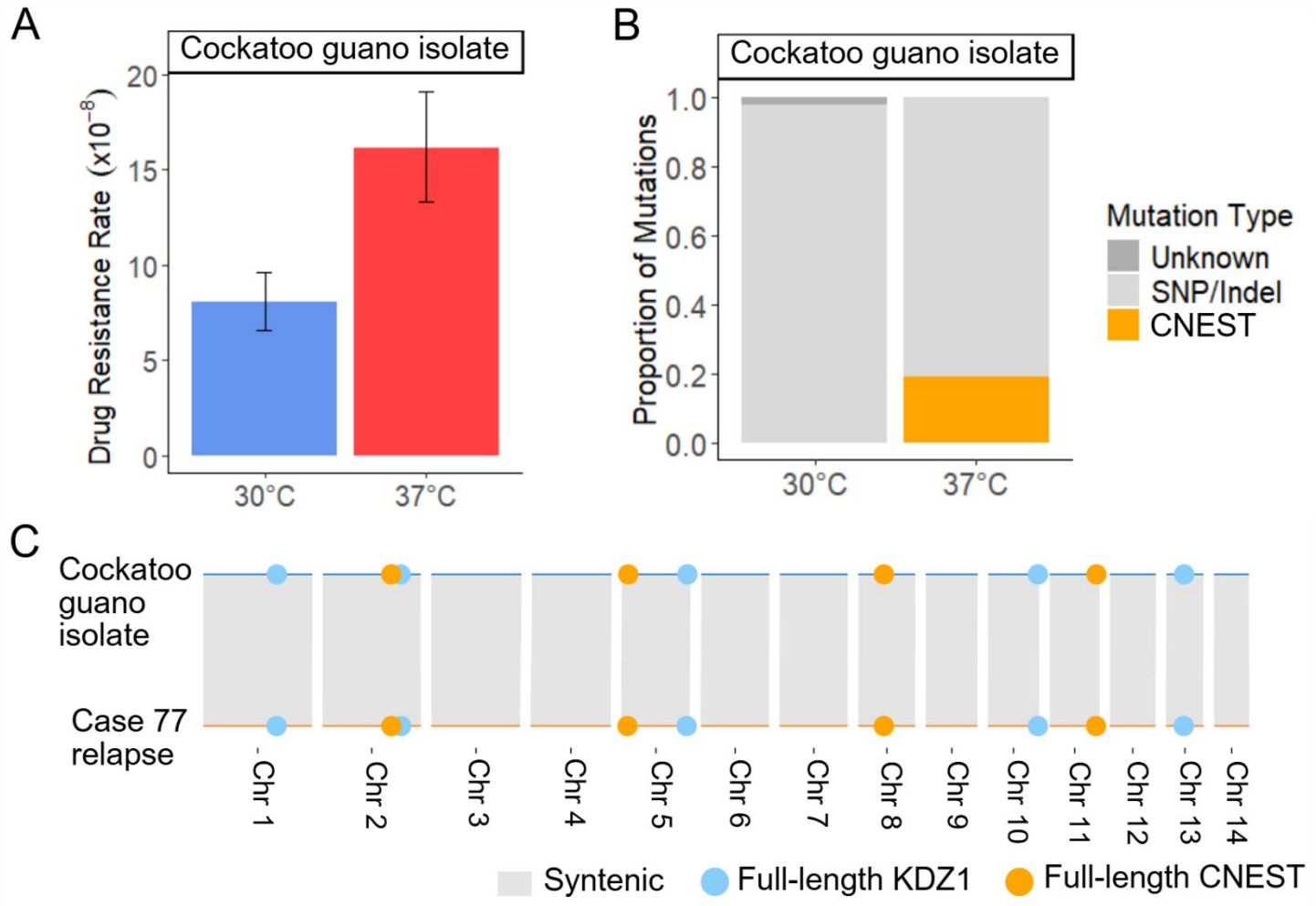

Figure 5. Heat stress-induced CNEST activation is conserved in an environmental isolate. (**A**) Rap+FK506 drug resistance rates following growth in non-selective YPD medium at 30°C or 37°C. (**B**) Mutation spectra in the *FRR1* gene for independent rap+FK506-resistant mutants. The mutation type "Unknown" indicates failure to amplify *FRR1* or absence of detectable mutations in its sequence (N = 42 – 52). (**C**) Chromosome-level synteny between the cockatoo guano and case 77 relapse isolates. Full-length copies of CNEST (yellow) and KDZ1 (light blue) are shown as circles.

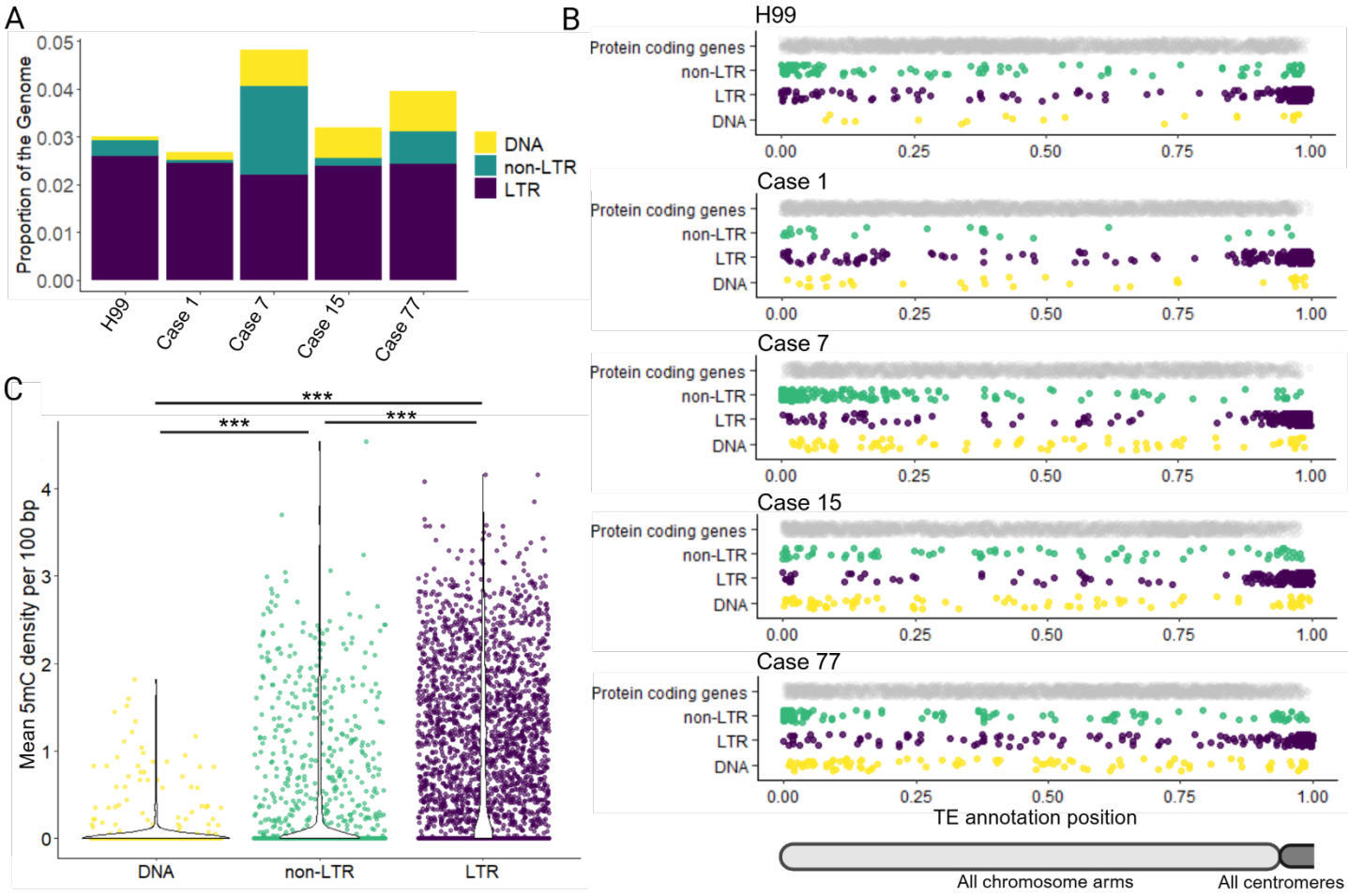

Figure 6. Genomic distribution and DNA methylation differ among non-LTR, LTR, and DNA transposons. (**A**) The proportion of the genome composed of non-LTR, LTR, and DNA transposons, based on the Earl Grey TE annotation. (**B**) Scaled positions of protein coding genes and non-LTR, LTR, and DNA transposons across chromosome arms. Chromosomes were split at the midpoint of the centromere region, and protein-coding gene and TE positions were scaled from 0 to 1 based on chromosome arm length. Data for all chromosome arms is plotted. (**C**) Mean 5mC DNA methylation density per 100 bp for DNA, non-LTR, and LTR TEs in isolates from cases 1, 7, 15, and 77. Violin plots are overlaid to illustrate the distribution. Significance was assessed using the pairwise Wilcoxon rank-sum test with continuity correction. *** denotes Bonferroni-adjusted $p < 2e\text{-}16$. The first genome assembly from serially collected clinical isolates was chosen as a representative for all cases.

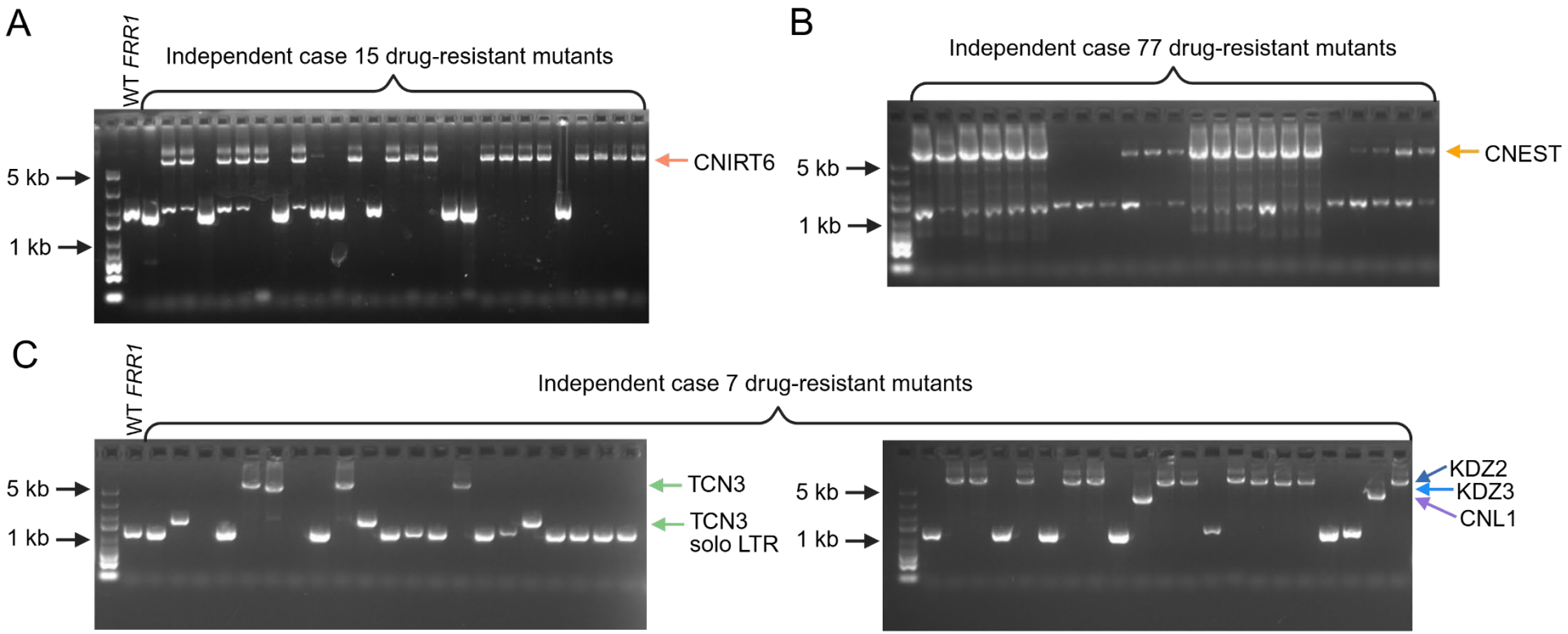

Figure S1. PCR amplification of *FRR1* in wild-type (WT) and independent rap+FK506-resistant mutants. *FRR1* was amplified from independent drug-resistant mutants from case 15 (**A**), case 77 (**B**), and case 7 (**C**); a subset of representative mutants is shown. Higher molecular weight bands indicative of TE insertion in *FRR1* were verified by Sanger or linear amplicon sequencing. Colored arrows indicate the molecular weights of bands identified as TEs.

A

```
cttgtccgtc acccctttcc ggagcggagg acctgcaata ctttccattc   60
ttctttcttc ttcttcATGT TCAGATCTAT CCTCACCACC TCTCGCCCCC  120
TCGTTAGACA GCCTCTCCGT CAATTTACTA CAACAGCTAT CAAAATGGGT  180
GTTACTGTTG AGgttggtat cttctgcttt ctcctagtga ccgatcggtc  240
cggagtgcat ctgagcgtca gtgctgatat gttgactgat ttttcttgcc  300
ttcaacagAA CATTTCCGCC GGTGACGGCA AGACCTTCCC CCAGCCTGGA  360
GACAATGTTA CTATCCACTg tgggttgtcc ttaaactccg cttcctgtgc  420
atctcgagat gagaacttgc aacactgaca tgatggcgac cttttgctat  480
gtaaatagAC GTTGGTACCC TTCTTGACGG TTCCAAGTTT GACTCTTCCC  540
GAGACCGTGG AACGCCCTTC GTCTGCCGAA TTGGCCAAGG gtaagtattt  600
ccgaaggtgc gcatatttca tagctgatac tgtttcgtag CCAAGTTATC  660
AGGGGTTGGG ACGAGGGTGT TCCTCAGCTC TCCGTAGGCC AGAAGGCTAA  720
CCTCATCTGT ACCCCTGACT ATGgtatgcg aagtttcttt cgttgcaaca  780
aattaaacct gacatctatc aattagCCTA CGGTGCGCGA GGTTTCCCCC  840
CTGTTATTCC TCCCAACTCC ACCCTCAAGT TCGAGGgtaa gtttgctctt  900
cgtcgacact acgtacctga cactgatttt tattacagTT GAGCTCCTCA  960
AGGTCAACTA AAatttattg cgtaaattag tagatggtct taaaagttag 1020
gaaatctgaa tgataagtga aagaagaatt aagtagacga tgatatgaac 1080
ggtgtggcga atgcttctaa acgtttcaaa attg
```

CNIRT6

B

CNIRT6 Insertion	TSD	Size of TSD
1	TAG	3
2	CGA	3
3	CTG	3
4	TAT	3
5	TTG	3
6	CAG	3
7	TTA	3

Figure S2. CNIRT6 insertion into *FRR1*. (**A**) A subset of CNIRT6 insertion sites (orange arrows) mapped in *FRR1*. The 5′ and 3′ untranslated regions (UTRs) of *FRR1* are underlined; introns are shown in lowercase, exons in capital letters, and the start codon is bolded. (**B**) TSDs detected at CNIRT6 insertion sites. Insertions are ordered based on their appearance in the *FRR1* sequence from beginning to end.

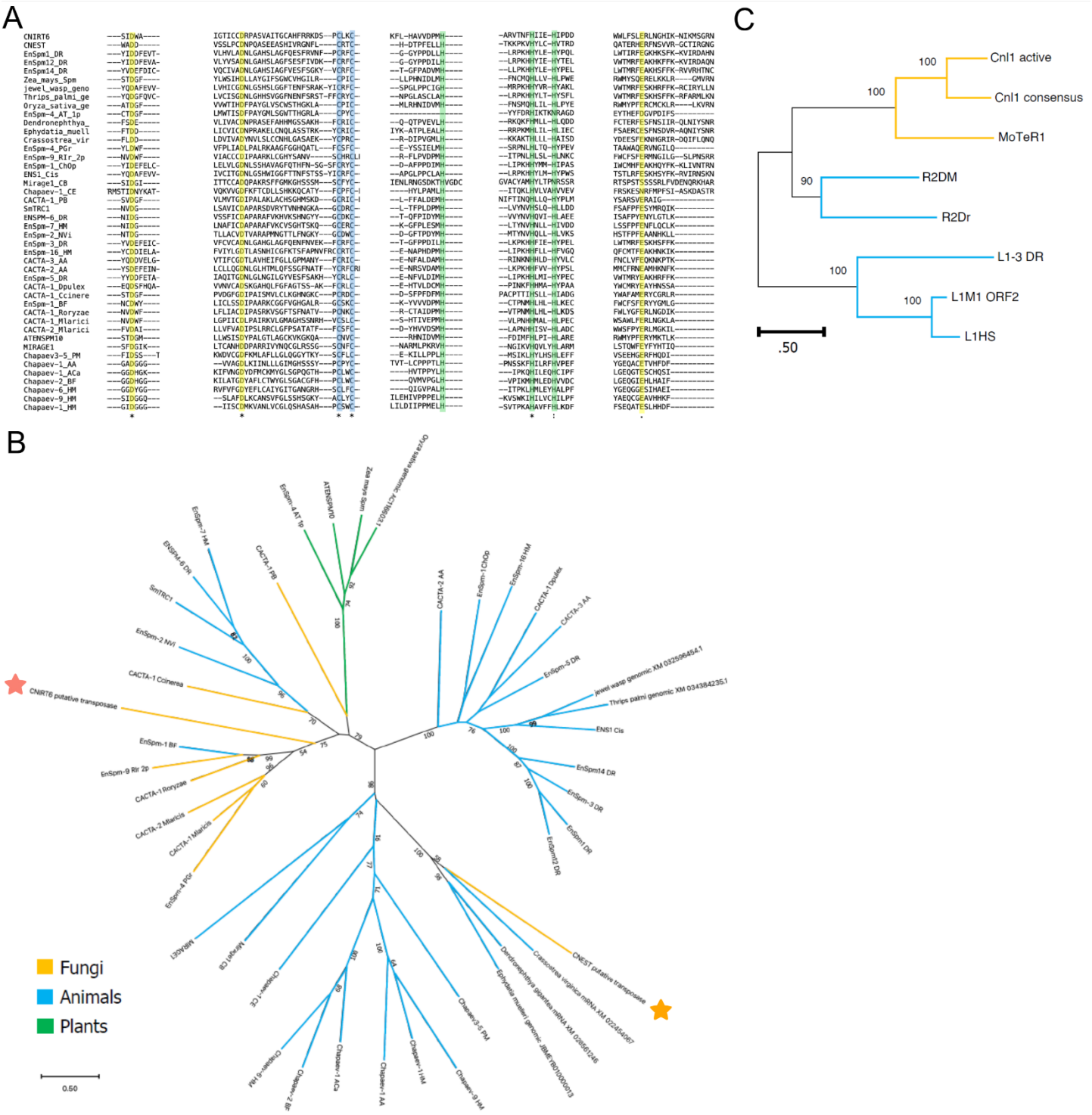

Figure S3. Classification of mobile CMC/EnSpm-like elements (CNIRT6, CNEST), and CNL1. (**A**) Regions of interest in a multiple sequence alignment highlighting conserved resides in CMC/EnSpm-like elements. Highlighted residues include the DDE catalytic core (yellow), conserved cysteine residues (blue) and conserved histidine residues (green) (42). (**B**) Unrooted amino acid phylogeny of diverse CMC/EnSpm transposases, demonstrating the relationship of CNIRT6 and CNEST with known CMC/EnSpm families and other related sequences. CNIRT6 is marked with an orange star, and CNEST with a gold star. (**C**) Unrooted amino acid phylogeny of reverse transcriptase domains, demonstrating the relationship between CNL1 and MoTeR1, and more distantly related R2 elements from flies and fish, as well as mammalian L1 elements. Branches are colored by kingdom: animals (blue), plants (green), and fungi (yellow). Bootstrap values greater than 50% are shown at nodes. Scale bars represent amino acid substitutions per site. Abbreviations: HS – *Homo sapiens*, DR – *Danio rerio*, DM – *Drosophila melanogaster*, CE – *Caenorhabditis elegans,* CB – *Caenorhabditis briggsae*, PM – *Petromyzon marinus*, BF – *Branchiostoma floridae*, , Dpulex – *Daphnia pulex*, Cis – *Ciona intestinalis*, Aca – *Aplysia californica*, Sm – *Schistosoma mansoni*, AA – *Aedes aegypt*, ChOp – *Chionoecetes opilio*, Jewel wasp – *Nasonia vitripennis*, Nvi – *Nasonia vitripennis*, HM – *Hydra magnipapillata*, Ccinerea – *Coproniopsis cinerea*, RIr – *Rhizophagus irregularis*, Roryzae – *Rizopus oryzae*, Mlaricis – *Melampsora laricis*, PGr – *Puccinia graminis*, PB – *Phycomyces blakesleeanus*, Mo – *Magnaporthe oryzae*, AT – *Arabidopsis thaliana*.

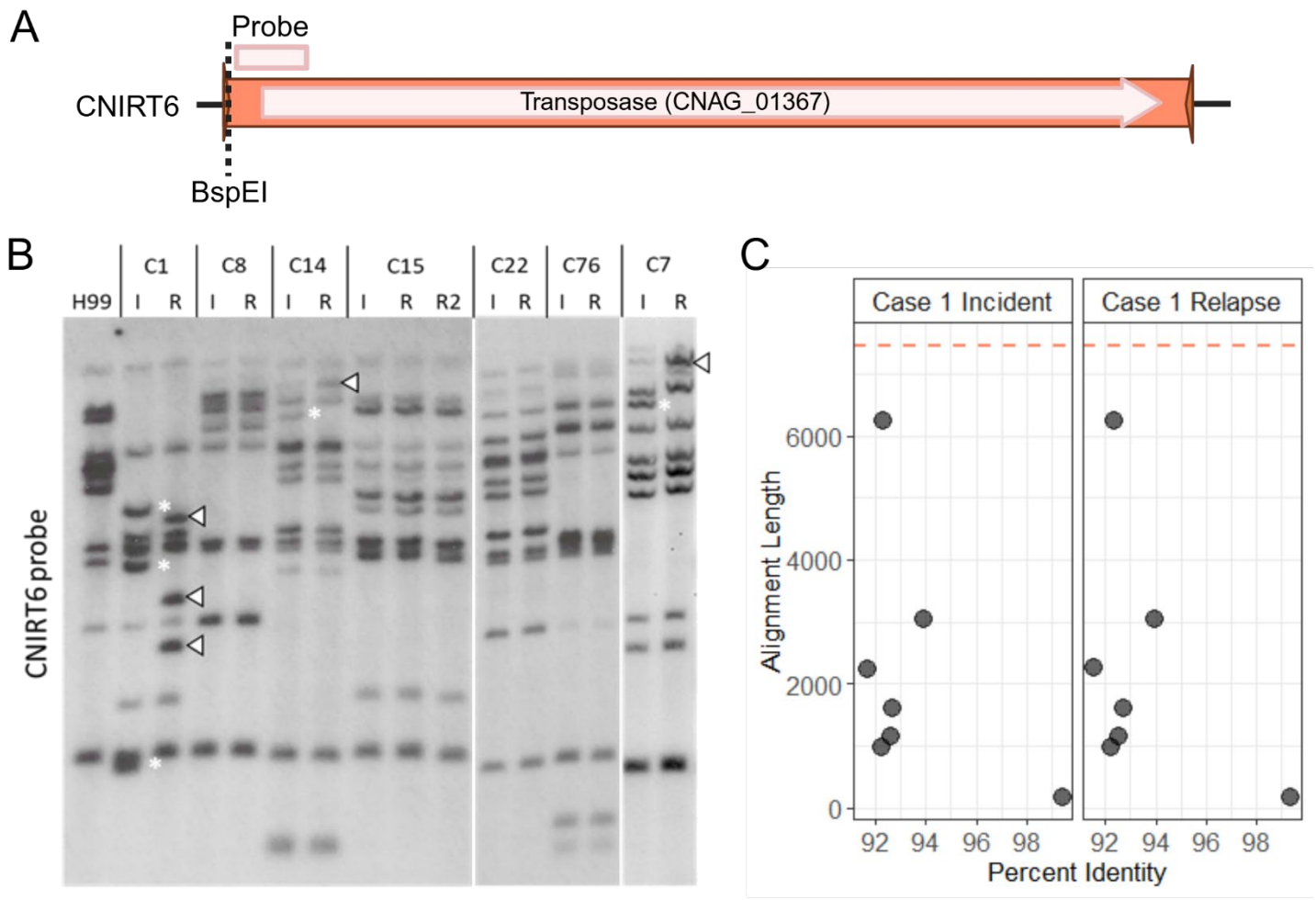

Figure S4. Putative CNIRT6 transposition events in serially collected clinical isolates. (**A**) Location of the restriction site (dotted line) and CNIRT6-specific probe used in Southern analysis. (**B**) Southern blot of genomic DNA digested with BspEI probed for CNIRT6 in incident (I) and relapse (R) isolates; case numbers are indicated as C#. Asterisks denote the loss of CNIRT6 fragments, while arrowheads indicate the emergence of CNIRT6 fragments at new genomic locations between incident and relapse isolates. (**C**) BLAT hits identified in case 1 isolates using full-length CNIRT6 as the query. The orange dashed line indicates the length of full-length CNIRT6.

A

```
ctcgtccgtc acccctttcc ggagcggagg acctgcaata ctttccattc   60
ttctttcttc ttcttcATGT TCAGATCTAT CCTCACCACC TCTCGCCCCC  120
TCGTTAGACA GCCTCTCCGT CAATTTACTA CAACAGCTAT CAAAATGGGT  180
GTTACTGTTG AGgtcggtat cttctgcttt ctccttagtg accgatcggt  240
ccggagtgca tctgagcgtc agtgctgata tgttgactga tttttcttgc  300
cttcaacagA ACATTTCCGC CGGTGACGGC AAGACCTTCC CCCAGCCTGG  360
AGACAATGTT ACTATCCACT gtgggttgtc cttaaactcc acttcctgtg  420
catctcgaga tgagaacttg caacactgac atgatggcga ccttttgcta  480
tgtaaatagA CGTTGGTACC CTTCTTGACG GTTCCAAGTT TGACTCTTCC  540
CGAGACCGTG GAACTCCCTT CGTCTGCCGA ATTGGCCAAG Ggtaagtatt  600
tccgaaggtg cgcgtacttc attagctgat actgtttcgt agCCAAGTTA  660
TCAGGGGTTG GGACGAGGGT GTTCCTCAGC TCTCCGTAGG CCAGAAGGCT  720
TAACCTCGTC TGTACCCCTG ACTACGgtat gcgaagtttc tttcgttgca  780
acaaattaaa cctgacatct atcaattagC CTACGGTGCG CGAGGTTTCC  840
CCCCTGTTAT CCCCCCCAAC TCCACCCTCA AGTTCGAGGg taagtttgct  900
cttcgtcgac actacgtacc tgacactgat ttttattaca gTTGAGCTCC  960
TCAAGGTCAA CTAAaatttt ttgcgtaaat tagtagatgg tcttaaaagt 1020
taggaaatct gaatgatagt ggaagaagaa ttaagtagac gatgatatga 1080
acggtgtggc gaatgcttct aaatgtttca aaattgcatt gct        1140
```

B

CNEST Insertion	TSD	Size of TSD
1	TA	2
2	TA	2
3	TA	2
4	TA	2
5	TA	2
6	TA	2
7	TA	2
8	TA	2
9	TA	2
10	TA	2
11	TA	2
12	TA	2

KDZ1 Insertion	TSD	Size of TSD
1	GAGCGTCA	8

CNEST
KDZ1

Figure S5. CNEST and KDZ1 insertion into *FRR1*. (**A**) A subset of CNEST (gold) and KDZ1 (light blue) insertion sites are mapped with arrows in *FRR1*. The 5′ and 3′ untranslated regions (UTRs) of *FRR1* are underlined; introns are shown in lowercase, exons in capital letters, and the start codon is bolded. (**B**) TSDs detected at CNEST and KDZ1 insertion sites. Insertions are ordered based on their appearance in the *FRR1* sequence from beginning to end.

A

```
ctcgtccgtc acccctttcc ggagcggagg acctgcaata ctttccattc   60
ttctttcttc ttcttcATGT TCAGATCTAT CCTCACCACC TCTCGCCCCC  120
TCGTTAGACA GCCTCTCCGT CAATTTACTA CAACAGCTAT CAAAATGGGT  180
GTTACTGTTG AGgttggtat cttctgcttt ctccttagtg accgatcggt  240
ccggagtgca tctgagcgtc agtgctgata tgttgactga tttttcttcc  300
cttcaacagA ACATTTCCGC CGGTGACGGC AAGACCTTCC CCCAGCCTGG  360
AGACAATGTT ACTATCCACT gtgggttgtc cttaaactcc gcttcctgtg  420
catctcgaga tgagaacttg caacactgac atgatggcga ccttttgcta  480
tgtaaatagA CGTTGGTACC CTTCTTGACG GTTCCAAGTT TGACTCTTCC  540
CGAGACCGTG GAACTCCCTT CGTCTGCCGA ATTGGCCAAG Ggtaagtatt  600
tccgaaggtg cgcatatttc atagctgata ctgtttcgta gCCAAGTTAT  660
CAGGGGTTGG GACGAGGGTG TTCCTCAGCT CTCCGTAGGC CAGAAGGCTA  720
ACCTCATCTG TACCCCTGAC TATGgtatgc gaagtttctt tcgttgcaac  780
aaattaaacc tgacatctat caattagCCT ACGGTGCGCG AGGTTTCCCC  840
CCTGTTATTC CCCCCAACTC CACCCTCAAG TTCGAGGgta agtttgctct  900
tcgtcgacac tacgtacctg acactgattt ttattacagT TGAGCTCCTC  960
AAGGTCAACT AAaatttatt gcgtaaatta gtagatggtc ttaaaagtta 1020
ggaaatctga atgatagtga aagaagaatt aagtagacga tgatatgaac 1080
ggtgtagcga atgcttctaa atgtttcaaa attg
```

KDZ2
KDZ3
CNL1
TCN3

B

KDZ2 Insertion	TSD	Size of TSD
1	GCTTTCTC	8
2	CCTTAGTG	8
3	CCGA	4
4	CCGGAGTG	8
5	CAGTGCTG	8
6	AGTTATCA	8
7	GGGACGAG	8
8	GGTGTTCC	8
9	CAATTAGC	8
10	CTCAAGTT	8

KDZ3 Insertion	TSD	Size of TSD
1	CGGTCCGG	8
2	CCGGAGTG	8
3	TCTGAGCG	8
4	CAAGGGTA	8
5	TAGCTGAT	8
6	GCTGATAC	8
7	AAGTTATC	8
8	GTTGGGAC	8
9	TCTGTACC	8
10	GACA	4

CNL1 Insertion	TSD	Size of TSD
1	CA	2
2	A	1
3		0
4	CACC	4
5	CACCCCT	7
6	CACCCCTTTCC	11
7	CACCCCTTTCCGG	13
8		0
9	ATCAGGGGT	9

TCN3 Insertion	TSD	Size of TSD
1	CTGAG	5
2	TGTTG	5
3	TGTTG	5
4	TTTGC	5
5	GTTTC	5
6	TTATC	5
7	GGGTG	5
8	GCTAA	5
9	CCTAC	5
10	GAGGG	5

Figure S6. KDZ2, KDZ3, CNL1, and TCN3 insertion into *FRR1*. (**A**) A subset of KDZ2 (dark blue), KDZ3 (blue), CNL1 (purple), and TCN3 (green) insertion sites are mapped with arrows in *FRR1*. The 5′ and 3′ untranslated regions (UTRs) of *FRR1* are underlined; introns are shown in lowercase, exons in capital letters, and the start codon is bolded. (**B**) TSDs detected at KDZ2, KDZ3, CNL1, and TCN3 insertion sites. Insertions are ordered based on their appearance in the *FRR1* sequence from beginning to end.

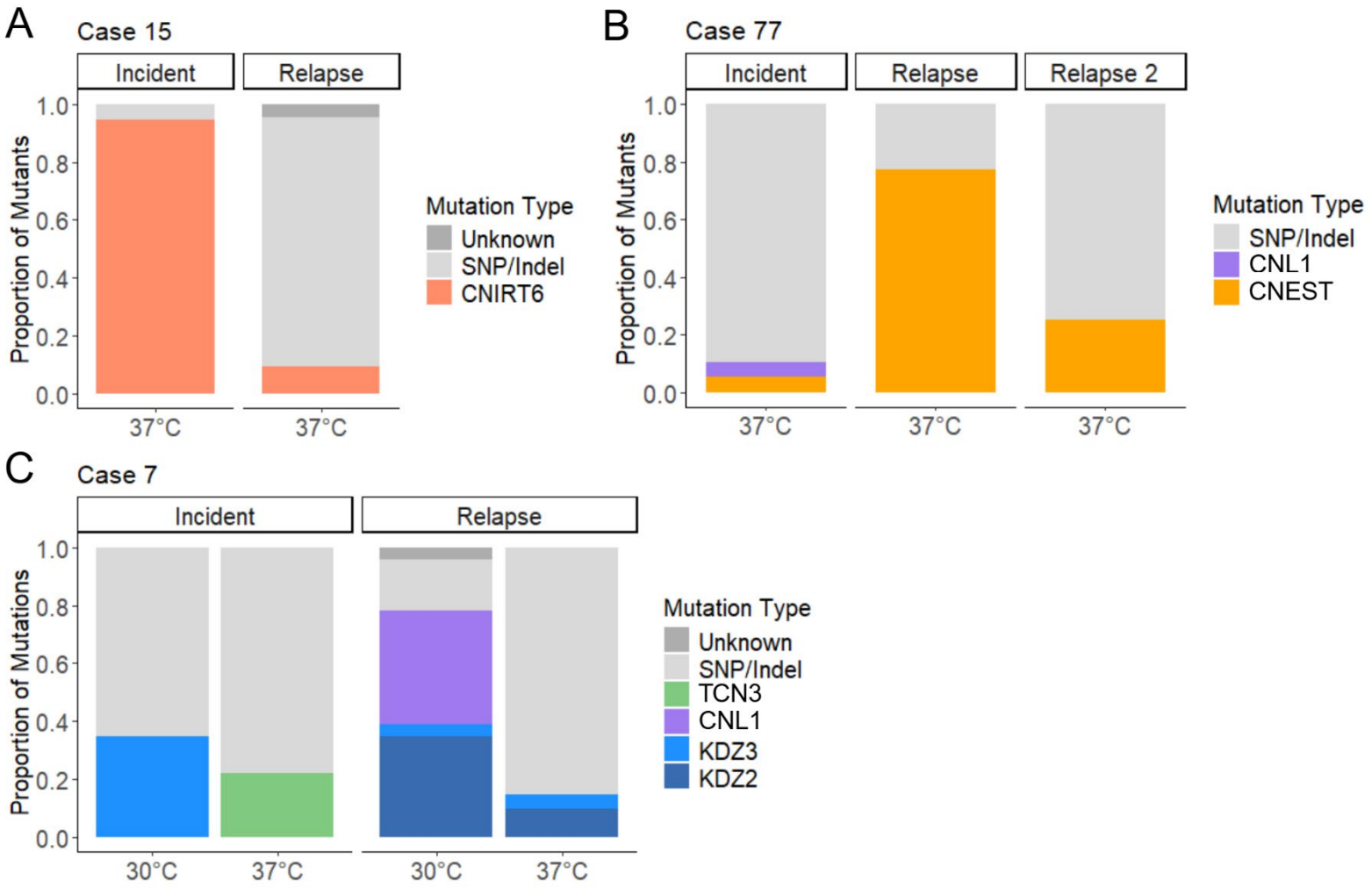

Figure S7. Limited nutrient availability alters TE mobilization dynamics. Mutation spectra in the *FRR1* gene for independent rap+FK506-resistant mutants in case 15 (**A**), case 77 (**B**), and case 7 (**C**). The mutation type "Unknown" indicates failure to amplify *FRR1* or absence of detectable mutations in its sequence (N = 18 – 31).

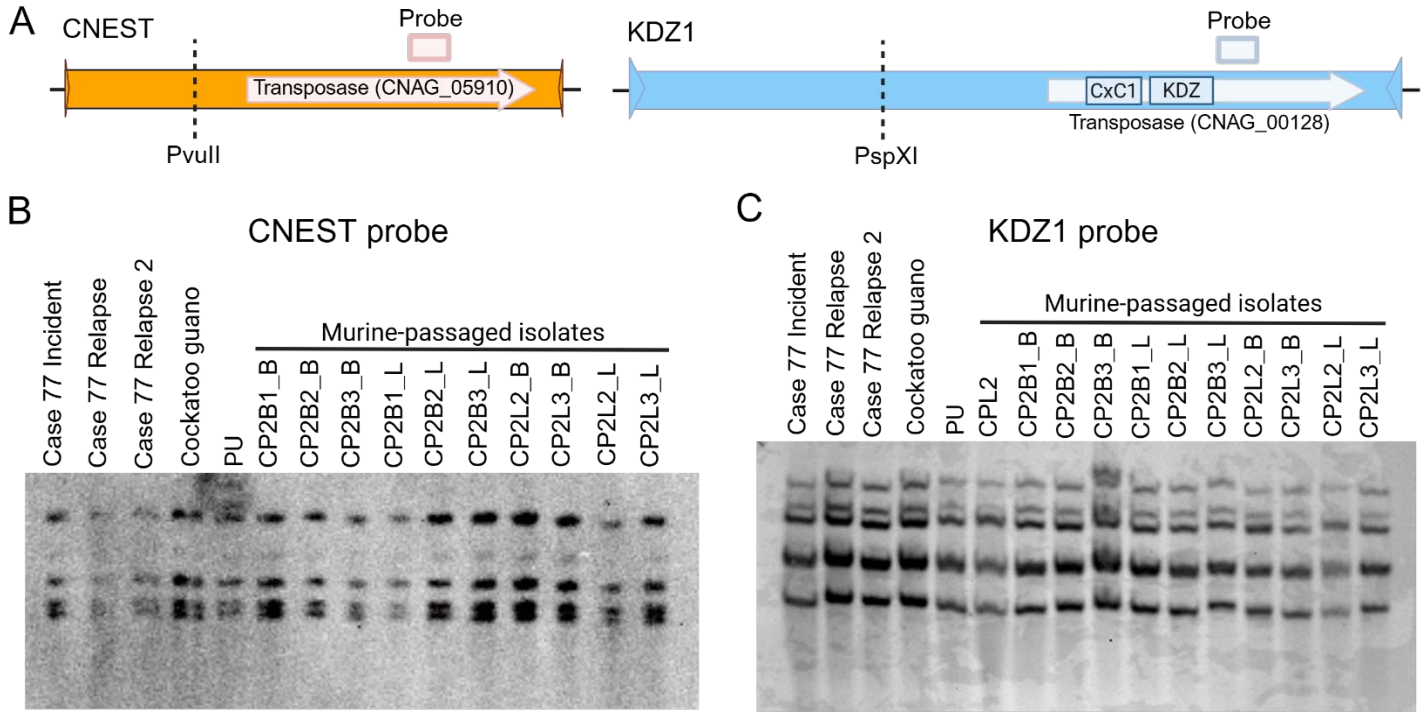

Figure S8. No predicted transposition of CNEST or KDZ1 in murine-passaged isolates. (**A**) Location of the restriction sites (dotted lines) and CNEST- and KDZ1-specific probes used in the Southern analysis. Southern blots of (**B**) PvuII-digested genomic DNA probed for CNEST, and (**C**) PspXI-digested genomic DNA probed for KDZ1. Shown are case 77 isolates, the cockatoo guano isolate, the patient isolate (PU) infected by the guano point-source strain, and cockatoo guano isolates passaged one to two times through mice by Sephton-Clark et al. (2023), recovered from brain or lung tissue (see Table S1 for strain details).

A

	CNIRT6	CNEST	KDZ1	KDZ2	KDZ3	CNL1	TCN3
Case 1 Incident	0	1	0	0	0	0	1
Case 1 Relapse	0	1	0	0	0	0	1
Case 7 Incident	0	1	1	3	2	16	2
Case 7 Relapse	0	1	1	3	2	39	2
Case 15 Incident	2	1	0	0	0	0	1
Case 15 Relapse	2	1	0	0	0	0	1
Case 15 Relapse 2	2	1	0	0	0	0	1
Case 77 Relapse	0	4	5	0	2	0	0
Case 77 Relapse 2	0	4	5	0	2	0	0
Cockatoo guano	0	4	5	0	1	0	0
H99	2	2	1	0	0	0	1

B

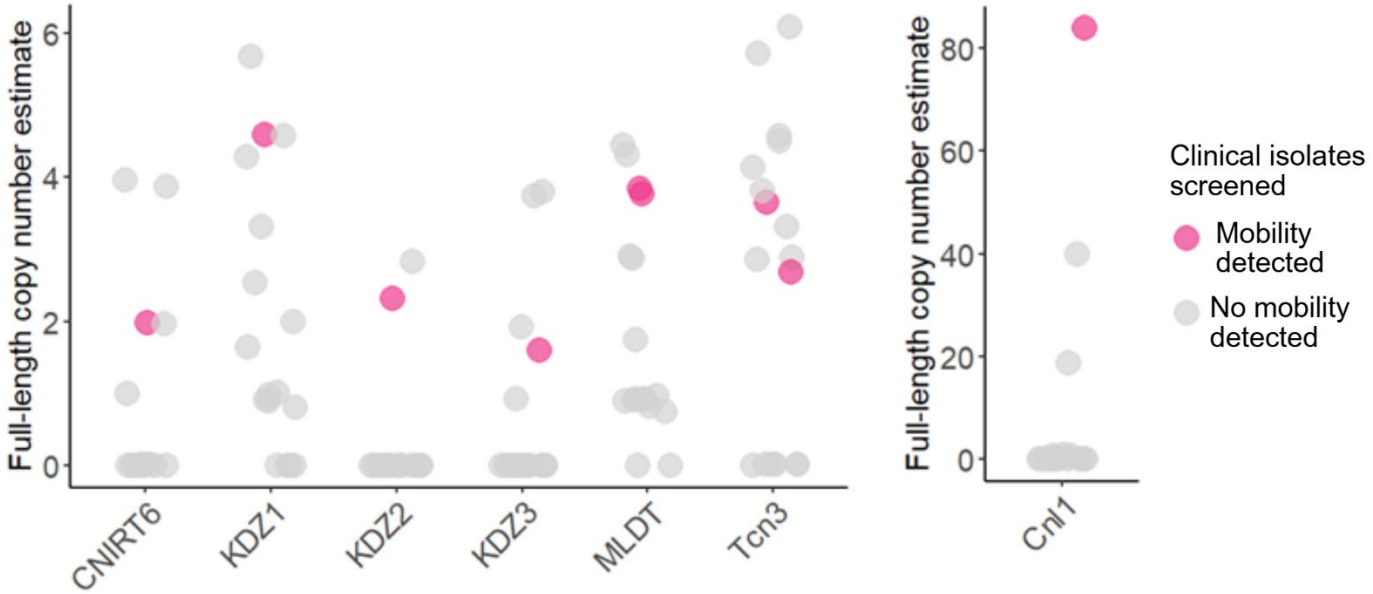

Figure S9. Full-length TE copies are present in genomes where no mobilization was detected. (**A**) Full-length TE copy numbers identified in whole-genome assemblies using BLAT and BLASTn homology searches. TE copy numbers in isolates with observed mobilization events are highlighted in pink. Isolate names are colored by lineage: VNI (blue), VNII (green), and VNBII (orange). (**B**) Full-length TE copy number estimates from short-read sequencing for all 15 *C. neoformans* incident isolates screened, isolates where no insertions were identified in *FRR1* are in grey, isolates where insertions were detected are in pink.

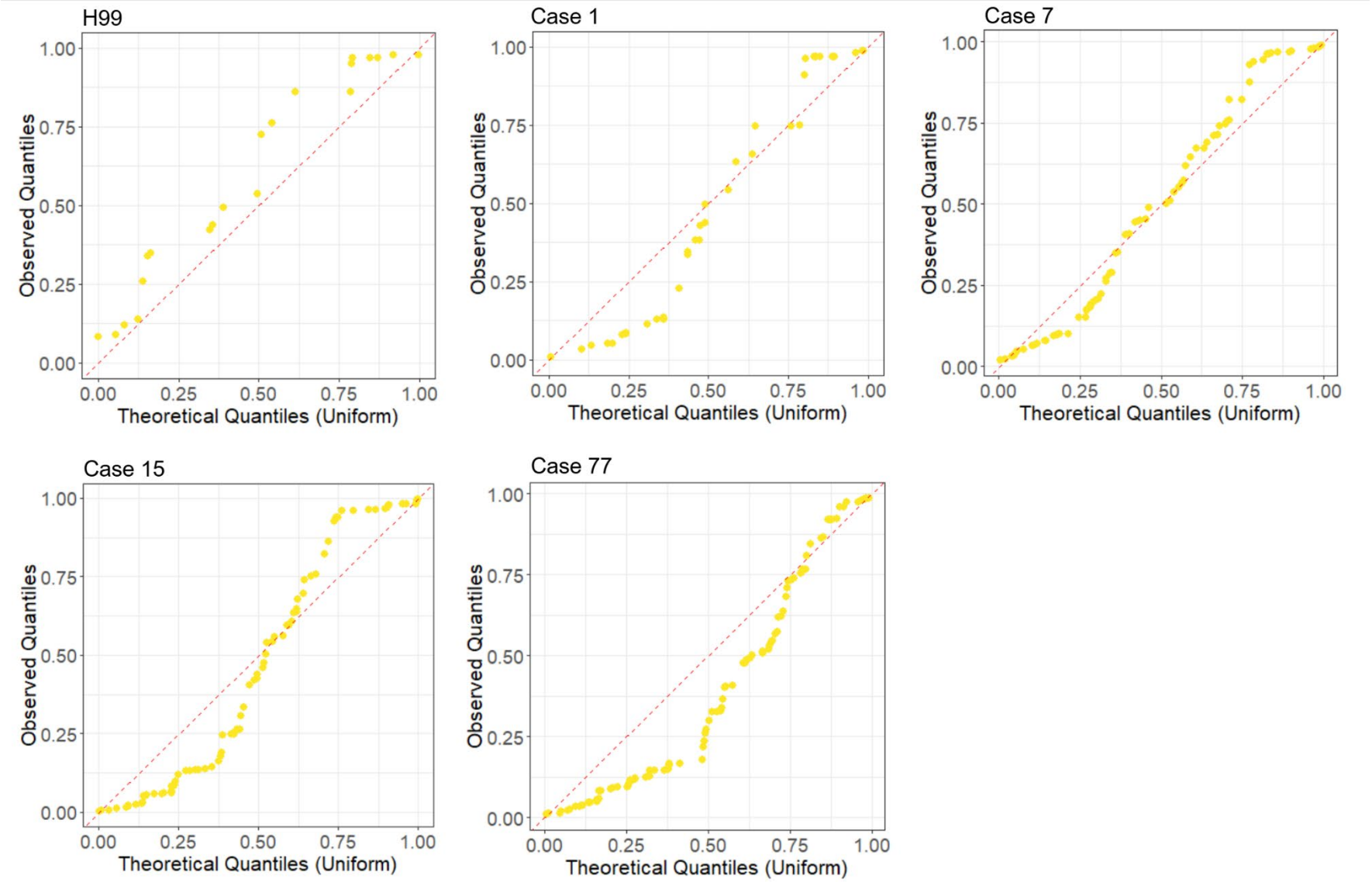

Figure S10. DNA TEs are approximately uniformly distributed across the genome. Quantile–quantile (QQ) plots are shown for the H99 reference genome and the first genome assembly from serially collected clinical isolates for cases 1, 7, 15, and 77 (representative examples). Observed quantiles correspond to the scaled positions (0 to 1) of DNA TEs along all chromosome arms. Theoretical quantiles are uniformly distributed random values between 0 and 1, sorted in ascending order, with their total number matching the number of observed DNA TEs.

A

Transposon type	Isolate	Total annotations	Percent methylated
LTR	Case 1	370	62.7
	Case 7	350	64.0
	Case 15	336	71.1
	Case 77	281	55.9
	Median	**343**	**63.4**
non-LTR	Case 1	25	8.0
	Case 7	223	53.4
	Case 15	74	8.1
	Case 77	204	37.7
	Median	**139**	**22.9**
DNA	Case 1	36	8.3
	Case 7	84	7.1
	Case 15	84	15.5
	Case 77	95	8.4
	Median	**84**	**8.4**

B

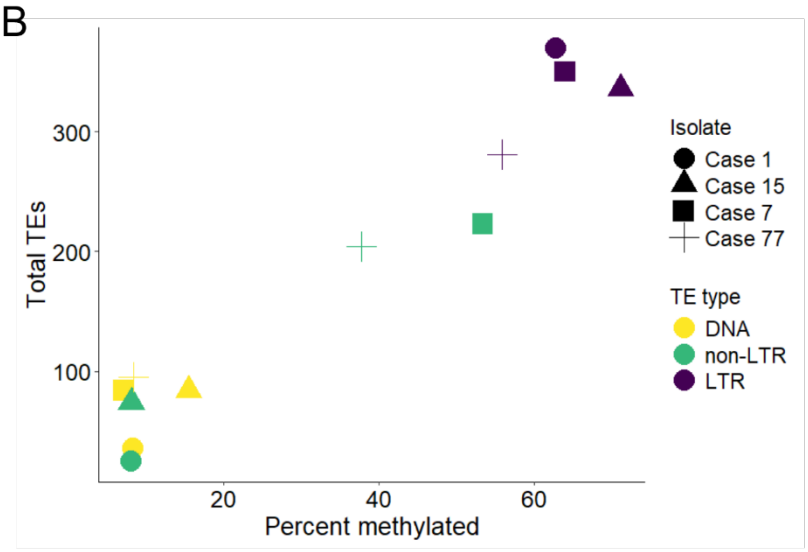

Figure S11. DNA transposons are less frequently methylated than LTR and non-LTR retrotransposons. (**A**) Number of TEs per type and the percentage containing at least one high-confidence DNA methylation call (methylation frequency > 0.75), with median values shown. (**B**) TE types (colors) per genome (shapes) and the percentage with at least one high-confidence DNA methylation call (methylation frequency > 0.75). The first genome assembly from serially collected clinical isolates was chosen as a representative.